AGU PUBLICATIONS

JGR

Journal of Geophysical Research: Solid Earth

RESEARCH ARTICLE
10.1002/2017JB014581

Key Points:
- Tensile and shear fractures are produced under uniaxial compression
- Tensile and shear fracturing show distinct microscopic characteristics
- The density and anisotropy of microcracks are analyzed quantitatively

Correspondence to:
L. N. Y. Wong,
lnywong@hku.hk

Citation:
Cheng, Y., & Wong, L. N. Y. (2018). Microscopic characterization of tensile and shear fracturing in progressive failure in marble. *Journal of Geophysical Research: Solid Earth*, *123*, 204–225. https://doi.org/10.1002/2017JB014581

Received 19 JUN 2017
Accepted 21 DEC 2017
Accepted article online 28 DEC 2017
Published online 17 JAN 2018

Microscopic Characterization of Tensile and Shear Fracturing in Progressive Failure in Marble

Yi Cheng[1,2] and Louis Ngai Yuen Wong[1,2,3]

[1]Faculty of Engineering, China University of Geosciences, Wuhan, China, [2]Formerly at School of Civil and Environmental Engineering, Nanyang Technological University, Singapore, [3]Department of Earth Sciences, University of Hong Kong, Hong Kong

Abstract Compression-induced tensile and shear fractures were reported to be the two fundamental fracture types in rock fracturing tests. This study investigates such tensile and shear fracturing process in marble specimens containing two different flaw configurations. Observations first reveal that the development of a tensile fracture is distinct from shear fracture with respect to their nucleation, propagation, and eventual formation in macroscale. Second, transgranular cracks and grain-scale spallings become increasingly abundant in shear fractures as loading increases, which is almost not observed in tensile fractures. Third, one or some dominant extensional microcracks are commonly observed in the center of tensile fractures, while such development of microcracks is almost absent in shear fractures. Microcracks are generally of a length comparable to grain size and distribute uniformly within the damage zone of the shear fracture. Fourth, the width of densely damaged zone in the shear fracture is nearly 10 times of that in the tensile fracture. Quantitative measurement on microcrack density suggests that (1) microcrack density in tensile and shear fractures display distinct characteristics with increasing loading, (2) transgranular crack density in the shear fracture decreases logarithmically with the distance away from the shear fracture center, and (3) whatever the fracture type, the anisotropy can only be observed for transgranular cracks with a large density, which partially explains why microcrack anisotropy usually tends to be unobvious until approaching peak stress in specimens undergoing brittle failure. Microcracking characteristics observed in this work likely shed light to some phenomena and conclusions generalized in seismological studies.

1. Introduction

The presence of fractures controls both cracking and mechanical behaviors of rock masses under loading. Early experimental studies have shown that the Griffith theory satisfactorily explains the initiation of tensile cracks from preexisting flaws (Bieniawski, 1967; Brace & Bombolakis, 1963; Olsson, 1974). Subsequent studies revealed that besides the tensile cracks, shear cracks (zones) can also be induced by a far-field compressive loading on specimens containing preexisting flaws. This result was reported on materials of plaster of Paris (Lajtai, 1971), Indiana limestone and granodiorite (Ingraffea & Heuze, 1980), polymethyl methacrylate and sandstone (Petit & Barquins, 1988), marble (Chen et al., 1995; Huang et al., 1990; Wong & Einstein, 2009a; Yang et al., 2008; Yang et al., 2009), and other natural rocks (Wong et al., 2006, 2007). All these studies suggested that two major crack types could initiate from a single preexisting flaw, namely, tensile crack (primary crack) and shear crack (secondary crack). Although various rock types containing different number of flaws have been tested extensively (Bobet & Einstein, 1998; Brace & Bombolakis, 1963; Horii & Nemat-Nasser, 1985; Ingraffea & Heuze, 1980; Petit & Barquins, 1988; Shen et al., 1995; Wong & Chau, 1998; Wong & Einstein, 2009b; Wong, Leung, & Wang, 2001; Yang et al., 2009), the observed crack types are similar to those initiating from a single flaw. As a summary, tensile and shear cracks have been regarded as two fundamental crack types in rock mechanics, though other terms of similar meanings have been used by some researchers interchangeably. Each of these cracks can be further divided into some subtypes, such as tensile wing crack and antiwing crack for tensile crack, and subcoplanar shear crack and oblique shear crack for shear crack. A systematic evaluation of these observed cracks was conducted by Wong and Einstein (2009a).

As established by previous studies, these two crack types are different in three main aspects. First, tensile cracks are produced by a tensile stress concentration even under a far-field compression loading condition (Bieniawski, 1967; Brace & Bombolakis, 1963; Griffith, 1924; Hoek, 1968), while shear cracks are produced by a compressive stress concentration (Chen et al., 1995; Lajtai, 1971; Petit & Barquins, 1988;

Wong et al., 2006; Wong et al., 2007). Second, tensile cracks may show various crack initiation direction with respect to the preexisting flaw, which are controlled by the stress field around the flaw. They usually propagate nearly parallel with the far-field compression direction and follow well-defined paths, which are characterized by observable openings. On the contrary, shear cracks usually have two possible orientations: subcoplanar or oblique with respect to the artificial flaw (normal to the compression direction has also been reported by Lajtai, 1971). Shear cracks often appear as damage belts or narrow zones consisting of many small scale cracks (Huang et al., 1990; Petit & Barquins, 1988; Sagong & Bobet, 2003; Wong & Chau, 1998; Wong & Einstein, 2009a). The trajectory of a shear crack is not well defined until final failure. Third, tensile crack surface is usually clean and smooth (Bieniawski, 1967; Horii & Nemat-Nasser, 1985; Huang et al., 1990; Lajtai, 1971; Petit & Barquins, 1988; Shen et al., 1995). However, shear cracks are usually characterized by a rough and stepped crack surface (Bobet & Einstein, 1998; Huang et al., 1990; Lajtai, 1971; Petit & Barquins, 1988; Shen et al., 1995; Wong & Einstein, 2009b).

While significant work has been conducted in the macroscopic observation and differentiation of tensile and shear cracks, only few studies focused on investigating these two crack types in the microscopic scale. Optical observation on the microcracking behavior of tensile cracks and the "subconjugate shear belt" confirmed that a tensile crack is featured by many grain boundary cracks while a shear belt is associated with many transgranualr cracks (Huang et al., 1990). Sagong and Bobet (2003) have drawn insightful conclusions by microscopically examining tensile and shear cracks in molded gypsum specimens under SEM (scanning electron microscope). Shear cracks often propagate along the crystal boundaries leading to a damage zone 5 to 10 times wider than tensile cracks, which mainly propagate along and across crystal boundaries. By applying a semiquantitative method, Wong and Einstein (2009c) reported that the microcracking zone of the wing crack extends and broadens as the loading progressively increases. Multiple microcracking zones oriented nearly parallel with the loading direction were also observed in the region between the preexisting flaw tips where a macroscale shear crack forms finally. However, the microscopic progressive development of a shear crack has rarely been observed and reported. As such, the development of grain boundary cracks and transgranular cracks involved in the tensile and shear cracks have been seldomly compared quantitatively. Although some quantitative microscopic studies have been conducted, they are mostly interested in the faulting mechanism or microcrack nucleation mechanism instead of comparing the tensile and shear cracks in detail (DiGiovanni et al., 2007; Menéndez et al., 1996; Moore & Lockner, 1995; Tapponnier & Brace, 1976; Wong, 1982, Yang, Tian, et al., 2017). Additionally, many seismic studies have explored the correlation between stress regimes (tensile or strike slip) and the non-double-couple components of the seismic events (Julian et al., 1998; Kwiatek et al., 2014; Stierle et al., 2014; Vavryčuk, 2002). These studies revealed possible correlations between AE (acoustic emission) events and modes of damage (compaction, shear, and cataclastic deformation) or loading conditions (Fortin et al., 2009; Stanchits et al., 2006). A few studies have also discussed the connections between fault structures (off-fault damage) and near-fault distributions of acoustic emissions (Goebel et al., 2014; Julian et al., 1998). All these studies definitely raise the awareness to characterize the tensional and shear fractures in microscale.

This study investigates the development of tensile and shear fractures (cracks) in marble specimens containing en echelon flaws of 30° and 90° inclination angle, respectively. After being loaded to different stress levels, the microcracking characteristics of these two configurations are examined in stages under an optical microscope. Specifically, the objectives of this study are to investigate: 1) the macroscopic and microscopic development processes of tensile and shear fractures, and 2) the density and anisotropy of microcracks, quantitatively.

The term "crack', which is only used in the introduction part to be in line with those macroscopic studies in this field, is replaced by "fracture' in the following sections to refer to a macro scale crack. This substitution aims to avoid possible confusion between the terms of crack and microcrack.

2. Material and Testing Procedures

2.1. Material Property

The natural rock, Carrara marble is chosen for this study because it is formed of 99% calcite crystals with only a few impurities. Marble was also used in previous studies for observation of microscopic deformation (Alber & Hauptfleisch, 1999; Fredrich et al., 1989; Li et al., 2005; Nolen-Hoeksema & Gordon, 1987; Olsson &

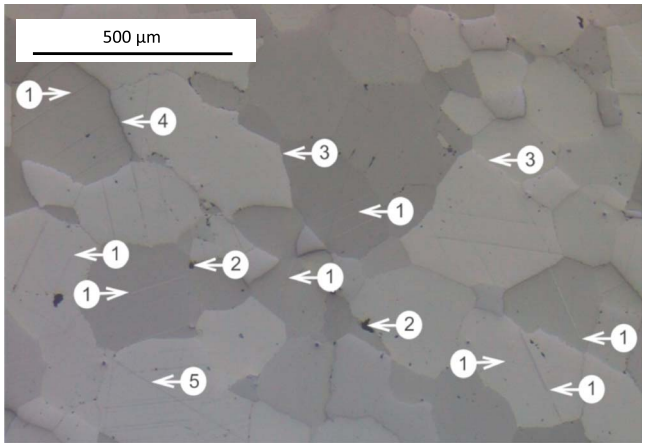

Figure 1. Photomicrograph of Carrara marble that has not been subjected to any experimental loading (plane polarized light). The labeled features are (1) tips of twin lamellae, which do not cross the whole grain; (2) void in grain boundaries; (3) microcrack-free boundary; (4) grain boundary crack; and (5) polishing mark crossing several grains.

Peng, 1976; Wong & Einstein, 2009c; Yang, Ranjith, et al., 2017). The overall porosity of Carrara marble is very low at a value between 0.3% (Alber & Hauptfleisch, 1999) and 1.1% (Edmond & Paterson, 1972). In this study, microscopic observations have been conducted on small cylinders cut from an intact marble slab to reveal the inherent grain structures and background microcracks of Carrara marble without experiencing any experimental loading (Figure 1). This rock is characterized by a mutually interfering growth pattern and a well-fused interlocking granoblastic polygonal texture (Figure 1). The grain size varies from 50 to 300 μm. Careful inspections also reveal that only a few microcracks and voids in grain boundary are present. No grains in Figure 1 show any observable transgranular microcracks. Prominent sets of twin lamellae are observed on more than half of the grains. Some twin lamellae do not cross the whole grain, while some appear segmented (Figure 1). The present observations suggest that they tend to be the preferential sites for the nucleation of microcracks under loading.

Uniaxial compression strength and Brazilian tensile strength of this rock dried at room temperature, are obtained in this study and are measured to be about 88.5 MPa (average value from four specimens) and 5.1 MPa (average value from seven specimens), respectively. The Young's modulus (49 GPa) and some other mechanical parameters can be found in another study conducted by Alber and Hauptfleisch (1999).

2.2. Specimen Geometry

Cuboid blocks are cut from marble slabs in dimensions of 152 mm height, 76 mm width, and 31–32 mm thickness. Multiple through-specimen (in thickness) en echelon flaws are then cut by the OMAX 2626 Waterjet. In accordance with previous studies (Eoin, 1988; Gehle & Kutter, 2003; Nicholson & Pollard, 1985; Pollard et al., 1982), the en echelon flaw configuration is defined by three parameters: array angle (θ), flaw inclination angle (β) and ligament length (L). The array angle (θ) is the acute angle between the minimum stress axis and the array trend; flaw inclination angle (β) is the angle between the minimum stress axis and flaw plane; ligament length (L) is the distance from the bottom tip of a flaw to the top tip of the neighboring flaw (Figure 2a). To produce localized damage zones of tensile and shear origins respectively, two flaw configurations are adopted in this study. These two configurations share the same array angle (θ = 60°) and ligament length ($L = a$ = 6.25 mm, where 2a is the flaw length), but different flaw inclination angles (β = 30° in Figure 2b

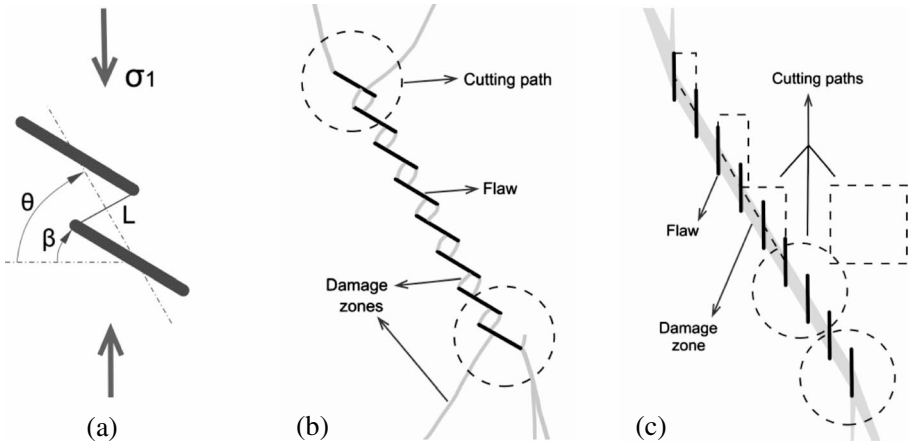

Figure 2. (a) Geometric parameters of flaw configuration: array angle (θ), flaw inclination angle (β), and ligament length (L). (b and c) Flaw configurations of β = 30° and β = 90°, respectively. In both images, the parallel thick lines indicate en echelon flaws; the shaded zones represent damage zones (microcracking zones) produced by uniaxial compression tests. Two or three cylinders (in dashed line) are cut from each prefailure specimen in both configurations, while four prisms (in dashed line) are sampled in the failed specimen of configuration (Figure 2b). These small samples containing some damage zones will be used for subsequent microscopic observation. Loading direction is vertical.

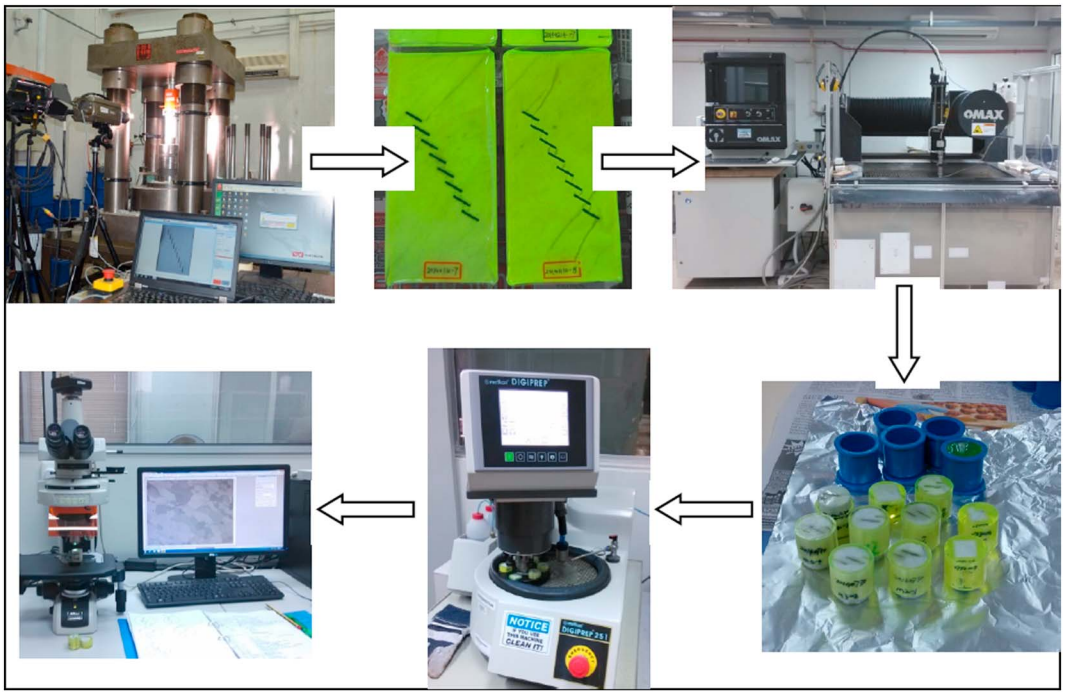

Figure 3. Experimental work flow to obtain microscopic observation results. These steps sequentially are uniaxial compression test, first coating (only specimens of $\beta = 30°$ shown here), sampling with the OMAX 2626 Waterjet, second coating (to obtain cylinders of a diameter close to 30.0 mm), polishing and microscopic observation.

and $\beta = 90°$ in Figure 2c). Previous studies have shown that en echelon flaws of $\beta = 30°$ would enhance the concentration of tensile stress and thus promote the development of tensile fractures, while en echelon flaws of $\beta = 90°$ have little interaction and may produce a throughgoing fault (Cheng et al., 2015; Hoek, 1968; Horii & Nemat-Nasser, 1985; Huang et al., 1990; Wong & Einstein, 2009b; Zhang et al., 2012). The important role played by the en echelon flaws of $\beta = 90°$ once was examined by some other researchers (Myers & Aydin, 2004, Peng & Johnson, 1972, Weiss & Schulson, 2009).

2.3. Testing Procedures

Six steps have been followed sequentially to obtain the microscopic results for specimens containing en echelon flaws. They are (1) uniaxial loading test, (2) first epoxy coating, (3) sampling, (4) second epoxy coating, (5) polishing, and finally (6) observation under microscope (Figure 3). Following sections will introduce them in turn.

All naturally dried cuboid specimens are loaded uniaxially at a rate of 0.05 mm/min. The uniaxial compressive strength tests are performed in the Rock Mechanics Laboratory at the Nanyang Technological University using a servo-controlled hydraulic rock compression system (Model STS-1000). The compression system has a maximum axial force of 4.45 MN and a frame stiffness of 5.25×10^9 N/m (Wong & Maruvanchery, 2016). The vertical displacement is measured by the linear voltage differential transducer and automatically logged by the operating system. The front face of the specimen is recorded by a Sony Camcorder (Sony HDR-XR150) and sometimes also a Phantom V310 high-speed video system (VRI-V310-16G-M). The latter can be triggered anytime to capture the abrupt fracturing events, such as the formation of a shear rupture.

Two sets of samples are uniaxially compressed. The first set is composed of three specimens of $\beta = 30°$ and five specimens of $\beta = 90°$. The second set is composed of several additional specimens possessing the same two configurations. In the first set, specimens are loaded to failure to observe the macroscale fracturing behaviors and to obtain the average peak stresses. All tested specimens of these two configurations show a good recurrence of damage zones, which are represented by the shaded bands in Figures 2b and 2c, respectively. In the second set, specimens are loaded to different ratios of the corresponding predetermined peak stress. Because the ratio of fracture initiation stress to peak stress in specimens of $\beta = 30°$ is much lower than that in

specimens of $\beta = 90°$, different loading schemes are applied to these two configurations to capture the microcracking process efficiently. For $\beta = 30°$, four specimens are loaded up to 20%, 50%, 75%, and 90% of its average peak stress respectively, while four specimens of $\beta = 90°$ are loaded up to 84.2%, 89.4%, 92.7%, and 100% (reaching failure) of its average peak stress, respectively. Samples were unloaded once these target stresses were reached.

Before sampling from the loaded specimens either by the OMAX 2626 Waterjet or a circular diamond saw, an epoxy-dye mixture is used to fill up the flaws and newly developed microcracks, as well as to coat the specimen surface (Figure 3). The epoxy can strengthen the loaded specimens against the cutting force due to waterjet or saw. By adding a Solvent Yellow fluorescent dye into the epoxy, microcracks filled with the epoxy will appear light violet or violet gray (depending on the magnification) under normal light and give a shining illumination under ultraviolet light. The coating process is performed inside a vacuum desiccator to promote the sucking of the epoxy mixture into the microcracks and pores of the specimen. After the solidification of epoxy, two cylinders of about 25.5 mm diameter, containing one to two bridges, are cut from each prefailure specimen and four prisms are cut from the failed specimen of $\beta = 90°$. The initial sampling locations for each configuration are shown in Figures 2b and 2c. If the polishing quality of some cylinders is not suitable for microscopic observation, supplementary specimens will be sampled again from the corresponding cuboid specimens.

If the size or shape of specimens does not fit into the holder of the polishing machine, they can be further coated (the second coating in Figure 3) after cutting to have a perfect geometry for polishing. Five polishing stages ranging from grinding, coarse polishing to fine polishing are then performed before microscopic examination. The abrasive diameters change progressively from 18 to 3 μm accordingly. The sixth stage, which cleans the specimen surface by using water as lubricant, aims to erase all possible scratches. At the end, the covering epoxy and a thin layer of rock will have been removed to produce a flat and smooth surface suitable for the subsequent microscopic observation.

The microobservation in the present study is conducted on the Nikon Eclipse LV100N polarizing microscope, which enables observations under both normal light and ultraviolet light (Figure 3). A digital camera (Nikon 165 Digital Sight DS-U3) is mounted to the microscope port to capture images of the observed scene on a light-sensitive sensor, which are then transferred to the computer. The installed software NIS-Elements 4.1 acquires the live stream of image from the camera for a live visualization of microscopic observations on the computer monitor. The software also allows a direct measurement of length and area on specified objects.

The optical microscope is used in the present study for two reasons. First, all grains and microcracks usually appear dark gray and black, respectively, under the SEM observation; thus, a SEM photograph tends to be inferior to an optical photomicrograph in terms of brightness and contrast. Most of all, identification of grain boundaries becomes difficult in rocks of a well-fused interlocking texture, such as marble (Cheng, Wong, & Maruvanchery, 2016; DiGiovanni et al., 2007; Nolen-Hoeksema & Gordon, 1987; Stanchits et al., 2009; Vajdova et al., 2012; Wong & Einstein, 2009c). On the contrary, because different calcite grains will show a different degree of grayish color, the optical detection is favored for identifying grain boundaries and thus distinguishing between grain boundary cracks and transgranular cracks. Second, as mentioned previously, Carrara marble has a grain size approximately between 50–300 μm, which is within the range of identification of the optical microscope. Therefore, to distinguish between grain boundary cracks and transgranular cracks in marble, a better contrast can be obtained by using the optical microscope than using SEM, as similarly suggested by some other researchers (Fredrich et al., 1989; Nolen-Hoeksema & Gordon, 1987).

3. Experimental Results

3.1. Failure Tests

The experimental results show that the average peak stresses (uniaxial compressive strength) are 22.1 MPa and 79.6 MPa for configurations of $\beta = 30°$ and $\beta = 90°$, respectively. The failure modes of the whole specimens are sketched in Figures 2b and 2c, while close-up views of the linking fractures are shown in Figures 4a and 4b.

According to results introduced in a number of previous studies (Bieniawski, 1967, Horii & Nemat-Nasser, 1985, Huang et al., 1990, Lajtai, 1971, Petit & Barquins, 1988, Sagong & Bobet, 2003, Shen et al., 1995), the

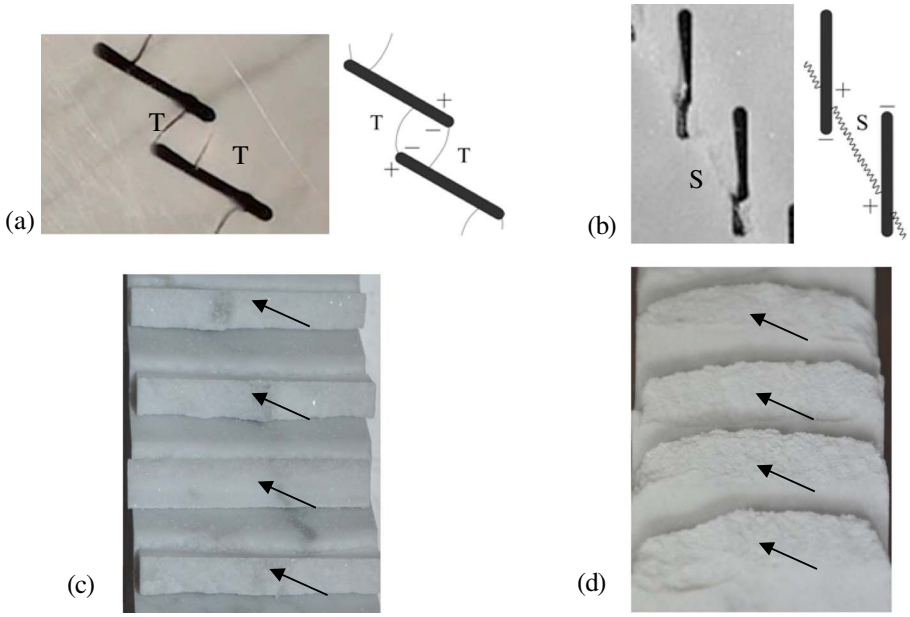

Figure 4. (a and b) Front view shows the path of linking fractures in specimens of $\beta = 30°$ and $\beta = 90°$ respectively (flaw length: 12.5 mm). "T" and "S" refer to fractures of tensile and shear origins, respectively. The plus and minus signs indicate the locations of compressive and tensile stress concentration respectively (vertical loading). (c and d) Fractures (pointed by arrows) in specimens of $\beta = 30°$ and $\beta = 90°$ are photographed to expose their surface topography. Photos were taken from the side of broken specimens so that the fractures were viewed face-on. The width of these photos equals the specimen thickness of about 31.5 mm.

linking fractures developed in specimens of $\beta = 30°$ can be identified as tensile fractures based on the following facts. First, these fractures develop in bridges where both flaws are subjected to local tensile stress concentration. Second, these fractures show an extensional deformation, which is associated with prominent openings (Figure 4a). Third, the interfaces of these fractures are very clean and light reflective, showing the original color of the fresh marble (Figure 4c).

Similarly, linking fractures developed in specimens of $\beta = 90°$ can be identified as shear fractures based on the following facts. First, these fractures develop in bridges dominated by local compressive stress (Cheng et al., 2015, Hoek, 1968). Second, these fractures show minute sliding but no openings upon approaching failure, and surface spallings are common (Figure 4b). Third, interfaces of these fractures are covered by a thin sheet of pulverized white powder, without the shining luster of the original calcite crystal (Figure 4d). These three characteristics agree with the studies on shear fractures conducted by previous researchers (Bobet & Einstein, 1998; Huang et al., 1990; Lajtai, 1971; Petit & Barquins, 1988; Sagong & Bobet, 2003; Shen et al., 1995; Wong & Einstein, 2009b).

3.2. Macroscopic Fracturing Process

The macroscopic fracturing in marble is preceded by the development of white patches (Chen et al., 1995; Li et al., 2005; Wong & Einstein, 2009b), which were proved to be microcracking zones under SEM observation conducted by Wong and Einstein (2009c). It implies that microdamage in marble usually changes its optical properties. In this study, the macroscopic fracturing processes in those two configurations have also been preceded by the development of white patches. Recordings from the camcorder and the high-speed camera suggest that the white patch development is different in these two flaw configurations. Specifically, bridges of extensional property ($\beta = 30°$) are characterized by the development of linear white patches, while bridges of contractional property are characterized by the development of diffuse white patches of a wider areal extent ($\beta = 90°$). Features of these two typical white patches and their progressive evolution to visible fractures will be described in detail below.

3.2.1. Stress-Strain Curve

Although the strain corresponding to the peak stress varies a lot among the test specimens, it can be generalized that the stress-strain curves of $\beta = 90°$ exhibit two features different from the curves of $\beta = 30°$ (Figure 5). First, compared with the initial loading stage (possibly a combination of emplacement and compaction

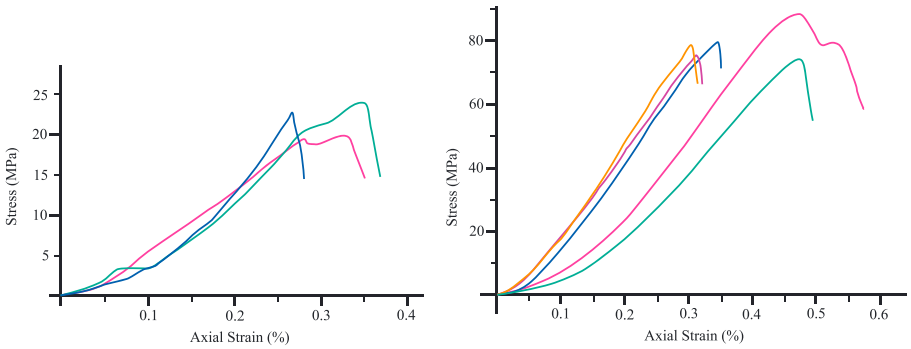

Figure 5. Stress-strain curves of specimens reach failure. Left: β = 30°, right: β = 90°.

stages), specimens of β = 90° show a significant increase in tangential modulus after this stage, while specimens of β = 30° only show a moderate increase. Second, after the initial loading stage, specimens of β = 90° usually deform linear-elastically under loading until the peak stress, while specimens of β = 30° demonstrate inelastic behavior even at an early loading stage, which is suggested by the nonlinear stress-strain curve.

In specimens of β = 30°, considerable fracturing events were often accompanied by a sudden increase of strain or transition of modulus in stress-strain curves. For example, the stress-strain curves show nonlinear behavior at an early loading stage (less than 5 MPa), which corresponds to the initiation and initial propagation of white patches (Figure 6b). After that, further loading probably results in the extension and widening of those white patches, which renders the increase of modulus difficult. It is probably why in specimens of β = 30° the modulus approaching peak stress is only moderately larger than that of the initial loading stage. On the contrary, the linear elastic behavior of β = 90° after the initial suggests that the specimens of β = 90° behave similar to an intact specimen loaded uniaxially. Their deformation stages should include perfect elastic deformation, stable microcrack proliferation and linkage, and unstable fracture propagation besides the initial compaction stage. It is why localized microcracking zone (white patch) cannot be observed until 70–80% loading of the peak stress (Figure 7b), and the modulus of linear-elastic stage is significantly larger than that of the initial loading stage.

3.2.2. Tensile Fracture (β = 30°)

Developed in extensional bridges, the linear white patch is a narrow whitening zone usually of a width no more than 0.5 mm. This zone is characterized by an observable contrast in color with the surrounding area (Figure 6). Therefore, the time of the initiation of linear white patches can be determined from camcorder recordings reliably. Camcorder recordings suggest that linear white patches appear when the applied stress ranges from 18% to 25% of the corresponding peak stress (Figure 6b). With the increase of loading up to about 30% of the peak stress, linear white patches extend quickly from the flaw periphery and connect with the neighboring flaw tips. After that, the white color is intensified as loading increases, but its width remains almost unchanged. Only about after 90% of the peak stress, fine fractures emerge from these white patches at the flaw periphery (Figure 6d). These fine fractures widen in aperture and extend to the neighboring flaw

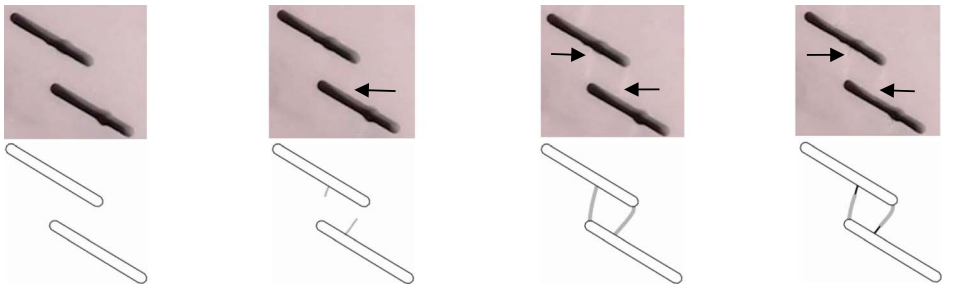

Figure 6. Images and sketches of the development of linear white patches with the increase of loading (β = 30°). Linear white patches and fine fractures are indicated by arrows (flaw length: 12.5 mm).

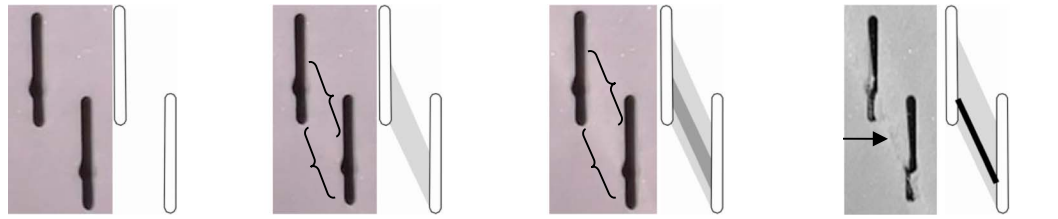

Figure 7. (a–d) Images and sketches of the development of diffuse white patches (indicated by brackets) and shear fractures (indicated by the arrow) with the increase of loading (β = 90°). The images in Figures 7a–7c are captured by the camcorder, while Figure 7d is captured by the high-speed camera (flaw length: 12.5 mm).

tips stably along the paths of linear white patches. Accompanying the final failure of the specimen, these fractures show prominent openings to link a flaw from its periphery with the neighboring flaw at its tip, such as those shown in Figure 4a.

3.2.3. Shear Fracture (β = 90°)

Developed in contractional bridges, the diffuse white patch is a whitening zone usually several times wider than the linear white patch (about 5.0–9.0 mm). Characterized by a gradual transition in color, the diffuse white patch has no distinct boundary with the surrounding area (Figures 7b and 7c). Therefore, it is very difficult to determine the exact time of the initiation of diffuse white patch. The best estimate of its appearance has been obtained by visually comparing images of loaded specimens with the image of the preloaded specimen repeatedly. Comprehensive examinations reveal that diffuse white patches appear quite late, approximately between 75% and 85% of the peak stress in specimens of β = 90° (Figure 7b). Intensification of white color and broadening of white zones are observed as loading increases progressively (Figure 7c). Approaching the maximum loading, sparkling and spalling appear on the specimen surface, indicating the pulverization of grains in a compressive stress field. Shear fractures are unobservable until reaching the peak stress. Unlike the stable development of fine fractures in the linear white patches, the development of shear fractures is so abrupt that only the high-speed camera can capture details of the cracking process. Note that even after the development of shear fractures, no opening between fracture interfaces can be observed (Figure 7d), which suggests that these fractures form in a compressive stress field.

The above macroscopic observations reveal that besides the different final fracture appearance, the tensile and shear fractures in marble are associated with the development of two different styles of white patches as well as stress-strain curves. The following sections will focus on the microscopic signatures of the two fracture types.

3.3. Microscopic Development of Tensile Fractures

Previous loading tests suggest that microcracking zones of tensile fractures appear as the applied stress reaches only about 20% of the peak stress. As such, for β = 30°, four specimens have been loaded up to 20%, 50%, 75%, and 90% of the average peak stress for microobservation. The microobservation results are illustrated in Figure 8.

Compared with the image captured from an intact specimen (Figure 1), optical observations in specimens loaded to 20% level reveal some damaged boundaries near flaw periphery (Figure 8a) and tip (Figure 8b). These boundaries only show minute openings, which have not produced any long dominant microcrack crossing multiple grains. At 50% stress level, continuous dominant microcracks have formed to link neighboring flaws. These epoxy-filled dominant microcracks appear light-violet color, which indicates an opening as wide as 28.0 ± 2.0 μm (Figure 8c). We fail to capture a transitional scene between 20% and 50% stress levels, which corresponds to the propagation of the dominant microcrack initiated from the flaw periphery toward the neighboring tip. With the increase of loading, no further microcracking events are observed besides the stable widening of the dominant microcracks. Corresponding to 75% and 90% stress levels, the dominant microcracks in Figures 8e and 8g show a width of 49.1 ± 5.0 μm and 70.4 ± 2.0 μm, respectively.

The appearances of microcracks near flaw peripheries are different from those near flaw tips. First, the former usually show a larger opening than the latter (Figures 8f and 8h and 8e and 8g). This distinction agrees with

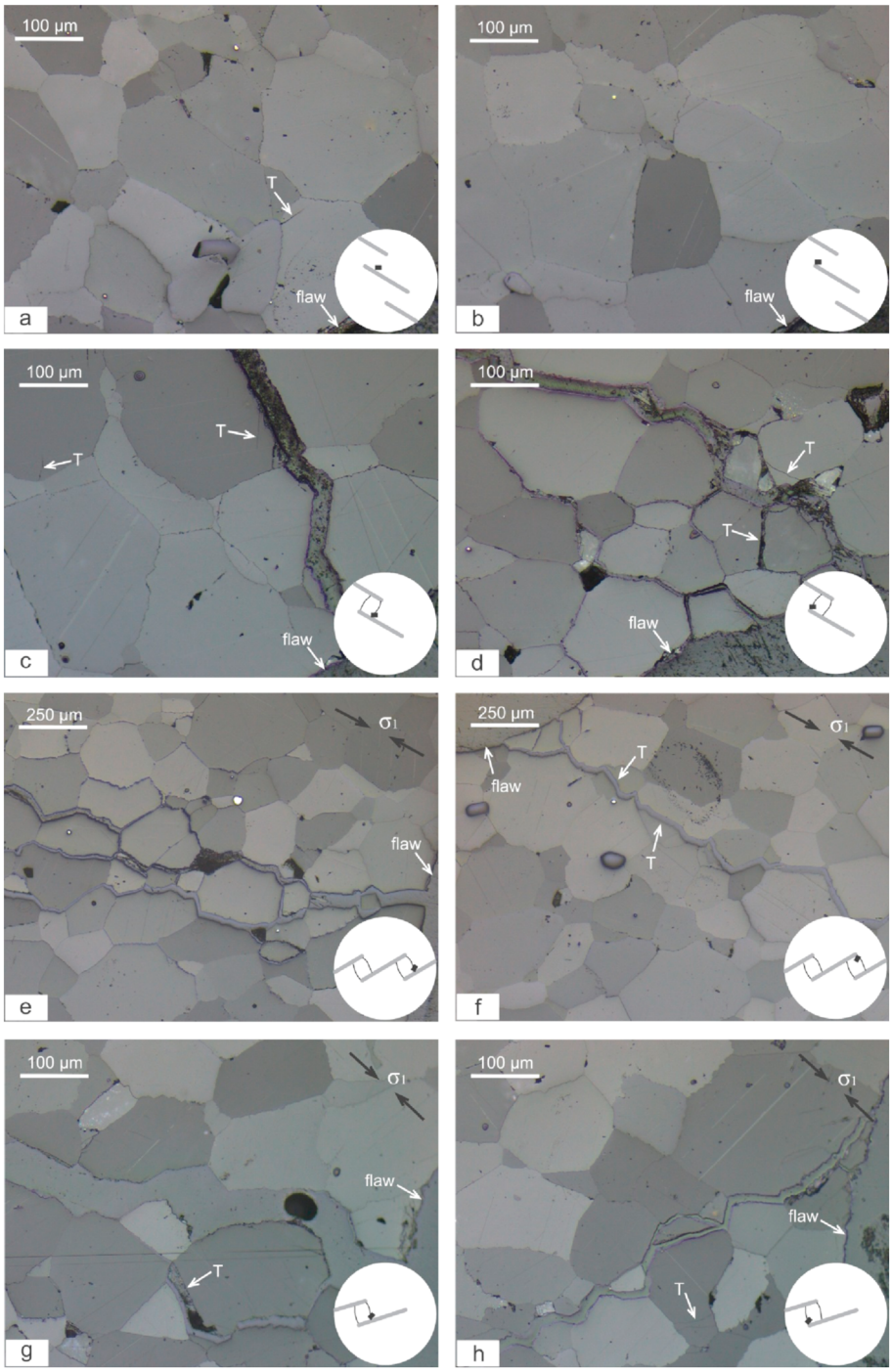

Figure 8. Development of microcracks in white patches of tensile fractures ($\beta = 30°$). The small black square in each white disk indicates the approximate location of each image, which suggests that all images in left column are captured at flaw peripheries while the right column are captured at flaw tips. (a–d) The loading direction is vertical, while (e–h) it is indicated by a pair of black arrows in top-right corner. Observable transgranular cracks in all images are labeled by "T', 20% stress level (Figures 8a and 8b): Some grain boundaries show a light degree of damage, 50% stress level (Figures 8c and 8d): Continuous dominant microcracks have been observed, while besides the dominant microcrack in Figure 8d, evenly distributed grain boundary cracks are found near the flaw tip, 75% stress level (Figures 8e and 8f): Some parallel branches developed from the main microcrack prefer a nearly horizontal orientation in Figure 8e, while a narrow dominant microcrack propagates into flaw tip in Figure 8f, 90% stress level (Figures 8g and 8h): The dominant microcrack near flaw periphery shows an opening much wider than that near flaw tip.

the macroobservation that tensile fractures first appear at the flaw peripheries and then propagate toward the neighboring flaw tips. Second, some observations reveal distributed damage zones around flaw tips where grain boundaries have cracked evenly and without preferred orientation (Figure 8d), while one or a

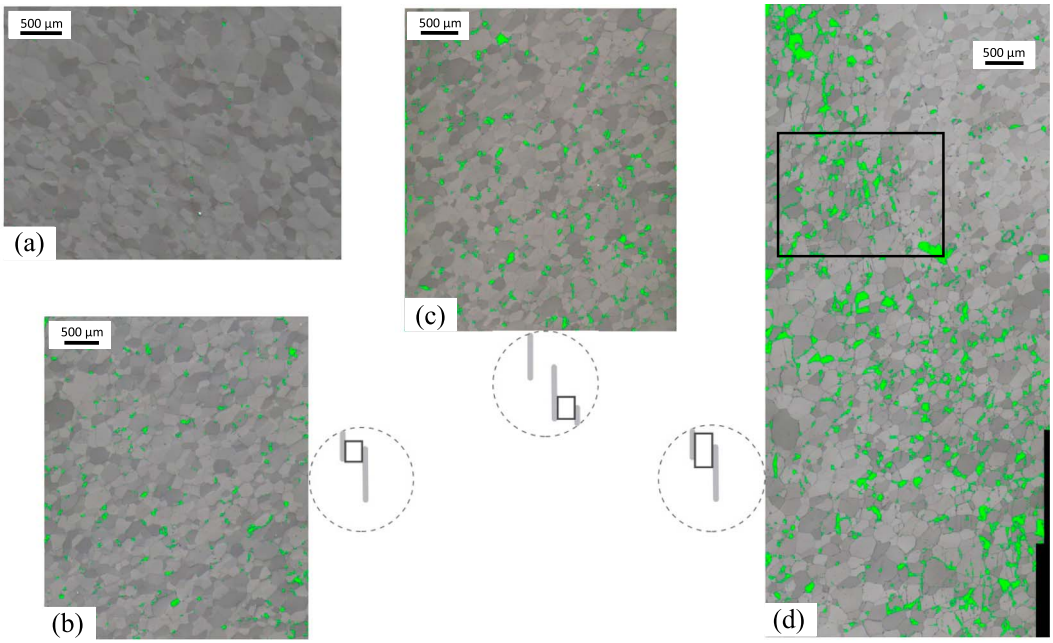

Figure 9. Development of areas of epoxy (in green color) in bridges of shear fractures (β = 90°, vertical loading). (a) In intact specimens, the green area occupies between 0.1% and 0.5% of the whole area. (b) The distributed green area occupies about 1.6% of the whole area after 82.4% loading. Note that most of the green area develops along grain boundaries. (c) At 89.4% loading, the green area occupies 2.8% of the whole area. Besides grain boundaries, some grains also show green color due to grain detachment (spalling). (d) Subjected to 92.7% loading, more broken grains and vertical microcracks have been filled with epoxy. The green area forms an inclined belt about 25° with the loading direction, which occupies 5.7% of the whole area. A zoom-in view of the rectangular area in Figure 9d is shown in Figure 10. The rectangles in three sketches indicate the locations of images in Figures 9b–9d, respectively.

few parallel dominant microcracks develop along certain preferred orientations near flaw peripheries (Figures 8c, 8e, and 8g).

Figure 8 reveals that within the damage zone of a tensile fracture, usually one or a few dominant microcracks of an opening about tens of microns will have developed. These dominant microcracks mainly consist of grain boundary cracks with a preferred orientation. They are flanked by other grain boundary cracks of minute openings (usually around 1 μm) distributed within 1 to 3 grains away from them. Microobservations of tensile fractures suggest that the damage zones are approximately 300 to 1,000 μm wide. Outside this zone, almost all grain boundaries seem to be tightly interlocked. Transgranular cracks have been found occasionally in all loading stages and labeled with "T" in Figure 8. Nonetheless, no evidence indicates that their occurrence increases as the increase of loading.

3.4. Microscopic Development of Shear Fractures

Loading tests show that microcracking zones of shear fractures appear as the applied stress is approximately over 75% of the peak stress. As such, for β = 90°, four specimens have been loaded up to 84.2%, 89.4%, 92.7%, and 100% (reaching failure) of the average peak stress for microobservation.

The primary microscopic feature of shear fractures is that the number of spalling grains and the opening of microcracks increase with the increase of loading. In Figure 9, the spalling grains and microcracks of large opening (of a width exceeding about 5 μm) are identified as epoxy patches, which are highlighted by green color manually. Most microcracks of small openings are thus ignored here. At stages of 82.4% and 89.4% stress levels, green patches still distribute evenly in bridges. After being subjected to 92.7% stress level, localized green patches form an inclined belt crossing the whole bridge. This belt is about 1.5 mm–3.0 mm wide and oriented about 25° with the vertical loading direction (Figure 9d). At this time, besides many spalling grains, the openings of some vertical microcracks are large enough to be highlighted by green color, which produces a corresponding ratio as large as 5.7%. On the other hand, Figure 9 shows that even at 92.7% stress level, the epoxy patches are mostly scattered without forming a continuous long microcrack, which commonly characterizes the damage zone of a tensile fracture in Figure 8.

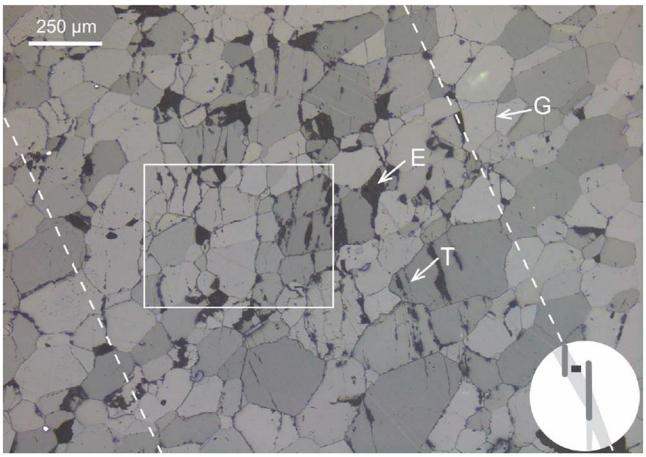

Figure 10. An overall view of the microstructures in the damage zone of a shear fracture: grain boundary crack (G), transgranular crack (T), and epoxy patch (E) (92.7% stress level, vertical loading). Only one of each microstructure is indicated as an example. A close-up view of the outlined rectangular area is shown in Figure 11d. The zone bounded by the two dashed lines is defined as the central part of damage zone. The black rectangle in the bottom-right disk indicates the approximate location of this image. The abundance of epoxy patches may be partly attributed to the fact that the observation was conducted on the free surface.

Second, the damage zone of a shear fracture consists of numerous evenly distributed grain boundary cracks and transgranular cracks. Before failure, no dominant continuous microcrack has been observed. An overall view of the central damage zone at 92.7% stress level is shown in Figure 10. Nearly all grain boundaries in this image have cracked, and these grain boundary cracks have a similar opening approximately between 1 μm and 3 μm. Over half of the grains in the central part of damage zone (between the dashed lines in Figure 10) have been fragmented by transgranular cracks, which now have openings comparable to those of grain boundary cracks. Unlike randomly oriented grain boundary cracks, the observed transgranular cracks tend to orient subparallel with the loading direction, and they are concentrated in the central part of damage zone. These two features, i.e., anisotropy and abrupt change of the microcrack density of transgranular cracks, will be quantitatively analyzed in the next section. However, regardless of the kind of microcracks, all of them seem to have developed discretely in the observed plane; almost none of them have been connected to form a long continuous microcrack of a large opening which is typical in the damage zone of a tensile fracture (Figure 8). Resulting from opening of microcracks and grain detachment, epoxy patches are also evenly distributed in the damage zone (Figure 10).

The third feature of the development of shear fractures is that transgranular cracks become increasingly populated as loading increases. After 82.4% loading, nearly all grain boundaries in the damage zone have been cracked, while short transgranular cracks have been observed occasionally (Figure 11a). Observations on specimens loaded to 89.4% level show little change in the opening of microcracks, while the number of transgranular cracks has increased in a modest manner (Figure 11b). After being subjected to 92.7% loading, all grain boundaries in the damage zone have cracked, and the number of transgranular cracks has increased significantly. The opening of microcracks, which has experienced an observable increase, is about 1–2 μm now (Figures 11c and 11d). Epoxy patches, which have filled the opening of microcracks and fragmentation of grains, thus become popular at this time. However, observations on the edge of a shear fracture reveal that epoxy patches have been found much fewer after failure (Figure 11e). It is probably because epoxy patches (spalling grains) are usually located in the central part of damage zone where the shear fracture finally develops. After failure, spalling grains and densely fragmented grains within the shear fracture will have detached from the specimen, which is suggested by a pile of white powder left by the failed specimens on the loading machine. If this inference holds, the final width of the shear fracture should be about 1.0–1.5 mm, which is the approximate width of the central damage zone (Figure 10). Taking the width of Figure 11e into consideration, the total width of damage area associated with shear fracture should exceed 5.0 mm after failure, which is comparable with the width of diffuse white patch obtained from macroscopic observation (Figure 6). Compared with Figures 11c and 11d, the most significant change revealed in Figure 11e is the considerable increase in openings of both grain boundary cracks and transgranular cracks, which usually range from 3 μm to 7 μm after failure, while some grain boundary cracks show an opening as wide as 15 μm. This should be attributed to the release of compression due to the presence of shear fracture.

Images in Figure 11 show the development of the cataclastic process zone. They indicate that a shear fracture appears only after many grains are fractured by microscopic extensional fractures. This phenomenon has been reported in sandstone and other porous rock types (Dunn et al., 1973; Menéndez et al., 1996; Petit & Barquins, 1988; Sagong & Bobet, 2003; Zhu et al., 2011) and suggested by AE characteristics in some crystalline rocks (Lei et al., 2000; Stanchits et al., 2006).

3.5. Microcrack Density

The length of microcrack was once used as a key parameter to characterize the microcrack density. Following studies suggested that such a length determination is to a certain extent subjective, since whether a long

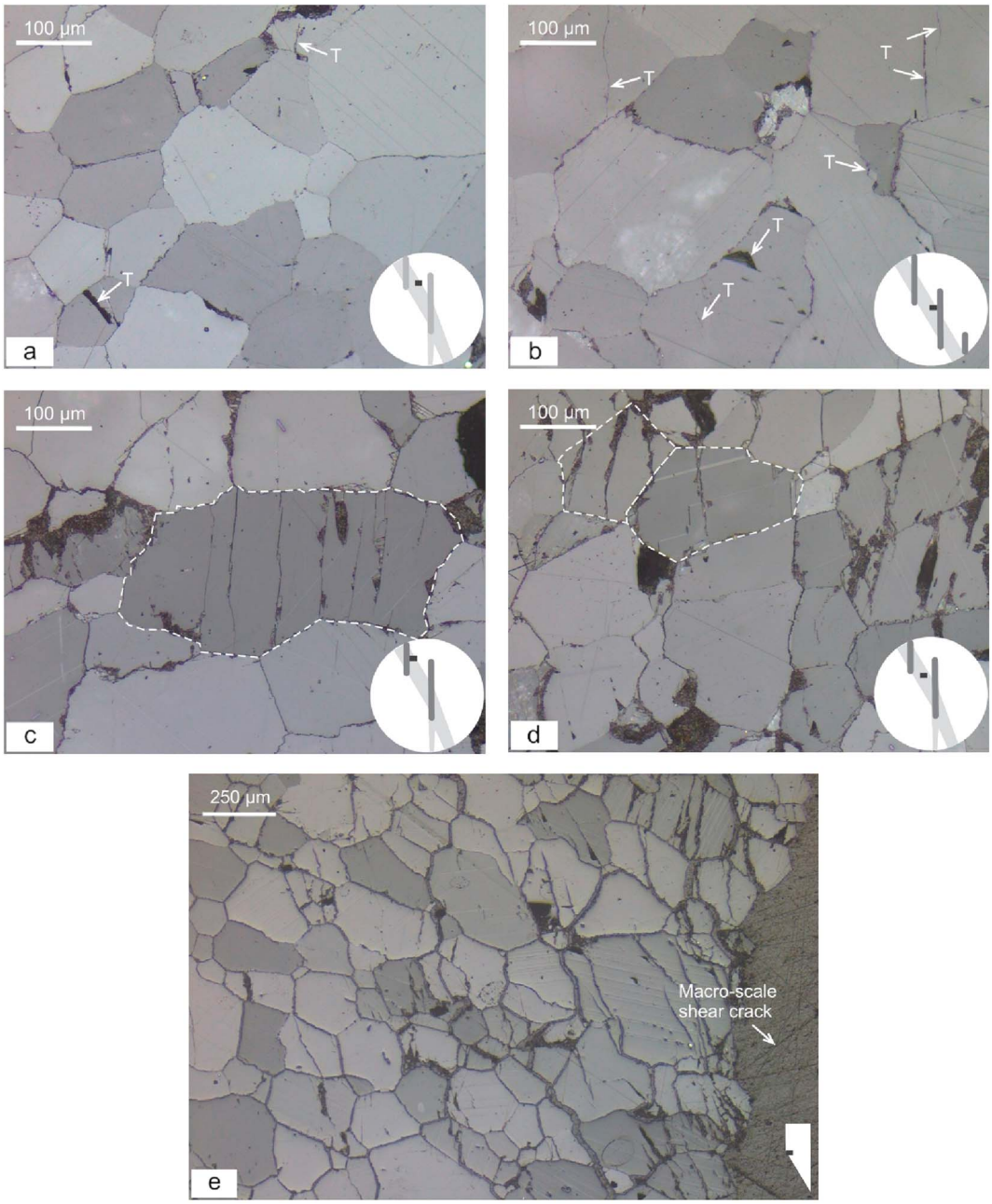

Figure 11. Development of transgranular cracks with the increase of vertical loading ($\beta = 90°$). (a) Only a few transgranular cracks are observed at 82.4% stress level. About half of the grain boundaries have totally cracked, and some others are partially cracked. All of them have minute openings of less than 1 μm. (b) At 89.4% level, some more transgranular cracks have appeared, while the opening of microcracks show little change. (c and d) Being subjected to 92.7% stress level, almost all grain boundaries in these two images have cracked. Some grains have been fragmented by multiple vertical microcracks, such as those outlined grains. Microcracks have shown an observable increase in opening. (e) After failure, the trace of a shear fracture has been identified by the epoxy infilling. Grain boundary cracks and transgranular cracks are not only abundant but also of large openings which are about 3–15 μm. The total width of this image is 2133 μm. Epoxy patches have become much fewer. Note that the scale in Figure 11e is different from other images.

zig-zag microcrack should be identified as a single microcrack or an assembly of short microcracks is subjected to the researcher's judgment (Bristow, 1960; Hadley, 1976; Homand et al., 2000; Moore & Lockner, 1995). This method also fails to reveal the anisotropy of induced microcracks. The stereological approach has later been adopted as an alternative for microcrack density characterization (DiGiovanni et al., 2007; Fredrich et al., 1989; Kranz, 1979; Menéndez et al., 1996; Tapponnier & Brace, 1976; Wong,

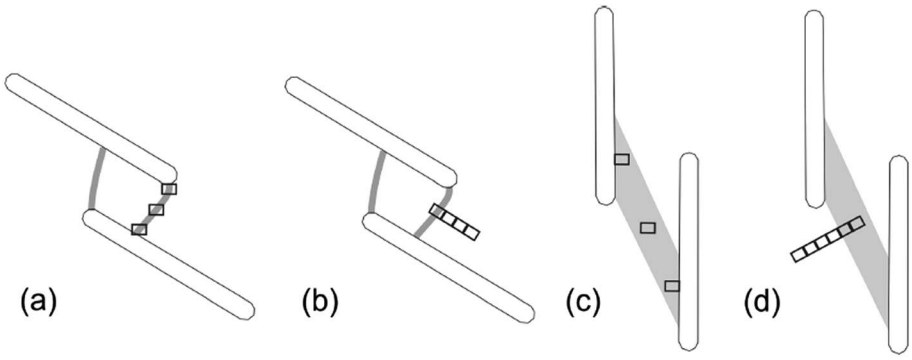

Figure 12. Approximate locations of the images (black rectangles) chosen for microcrack density measurement. (a and c) Three images located in the center and two ends of the corresponding white patch are measured (the first series). (b and d) Images aligned perpendicular to the corresponding white patch are measured (the second series). According to some published results (Figures 4 and 5 in Moore & Lockner, 1995, and Figure 7 in Vermilye & Scholz, 1998) and observations in this study, the damage zones are assumed to be approximately symmetrical. The second series is hereby conducted only at one side of the white patches. In the second series, besides these continuous images, one more image at a distance of about 12.0 mm from the core of damage zone is measured. See Table 1 for the number and locations of images measured.

1982; Wu et al., 2000). In this method, microcrack density P_L is expressed as the mean number of microcrack intersections for test lines of unit length:

$$P_L = N_{\text{tot}}/L_{\text{tot}} \tag{1}$$

where N_{tot} is the total number of intersections and L_{tot} is the total length of test lines. By aligning the test lines in parallel and perpendicular to the σ_1 (principal compressive stress) direction, microcrack densities in two orthogonal directions can be measured as $P_L^{\parallel}$ and $P_L{}^{\perp}$accordingly to examine the anisotropy.

Additionally, for axisymmetrically deformed specimens, the total microcrack surface area per unit volume, S_V, can also be determined by $P_L^{\parallel}$ and $P_L{}^{\perp}$ (Underwood, 1970; Wong, 1985):

$$S_V = \pi/2 \cdot P_L{}^{\perp} + (2 - \pi/2) \cdot P_L^{\parallel} \tag{2}$$

Two series of measurement have been implemented in the present study by adopting the stereological approach. The first series examines the microcrack density variation with respect to different stress levels for both linear and diffuse white patches. For each stress level, measurements are performed on three images in different locations to obtain an average value (Figures 12a and 12c). Thus, nine images are chosen from the linear white patches (50%, 75%, and 90% loading) and also nine images from the diffuse white patches (84.2%, 89.4%, and 92.7% loading). Each image is 871.4 μm in width and 652.6 μm in height. According to previous studies (Fredrich et al., 1989; Menéndez et al., 1996; Moore & Lockner, 1995; Tapponnier & Brace, 1976; Vajdova et al., 2010), especially for a localized damage zone, the measuring area is acceptable for obtaining reliable microcrack densities. The second series examines the variation of microcrack density with the distance away from the core of damage zones. Thus, the microcrack densities are measured in images perpendicular to the long axis of the white patch (Figures 12b and 12d). Each image in the second series is slightly smaller, which is 578.7 μm in width and 829.6–870.2 μm in height. Measurements in the second series are conducted on three sets of specimens: specimen containing linear white patches loaded up to 90% stress level, specimen containing diffuse white patches loaded up to 92.7% stress level, and specimen already experienced shear failure. Additionally, the microcrack density in Figure 1 has been measured as the background value. All the measurements are conducted along test lines at a spacing of 25 μm in two orthogonal directions across the whole image. The intersections of grain boundary crack and transgranular crack are recorded separately.

The stereological microcrack density data are listed in Table 1. Intact sample possesses a neglectable microcrack density, which is in accordance with the observation of Figure 1. Some of the other data are plotted in Figures 13 and 14 for a more intuitive visualization. In the damage zones of tensile fractures, the microcrack density seems not to increase with the increase of loading, and the degree of anisotropy is insignificant in the two directions: parallel ($P_L^{\parallel}$) and perpendicular ($P_L{}^{\perp}$) to the σ_1 direction (Table 1 and Figure 13a). These two generalizations are applicable to both grain boundary crack and transgranular crack. However, the total

Table 1
Stereological Microcrack Density Data[a]

Specimen type		D[b](mm)	$P_L^{\perp}$ (/mm)			$P_L^{\parallel}$ (/mm)			S_V (mm^2/mm^3)	Total (/mm)	
			BC[c]	TC[c]	Total	BC[c]	TC[c]	Total		BC[c]	TC[c]
Intact		/	/	/	/	/	/	/	/	0.4	0.0
Tensile fracture[d]	50%	0.00	5.0	0.9	5.9	3.9	1.0	4.9	12.1	8.9	1.9
	75%	0.00	3.4	0.2	3.6	3.3	0.3	3.6	7.7	6.7	0.5
	90%	0.00	5.6	0.3	5.9	5.7	0.3	6.0	12.7	11.3	0.6
Shear fracture	82.4%	0.00	5.1	0.6	5.7	5.6	0.4	6.0	12.4	10.7	1.0
	89.4%	0.00	4.7	1.7	6.4	4.4	0.6	5.0	12.9	9.1	2.3
	92.7%	0.00	6.4	7.2	13.6	6.4	3.3	9.7	26.9	12.8	10.5
Tensile fracture (90% of failure load)		0.00	5.9	0.1	6.0	5.0	0.1	5.1	12.3	10.9	0.2
		0.58	3.4	0.1	3.5	3.2	0.1	3.3	7.4	6.6	0.2
		1.16	3.2	0.0	3.2	2.7	0.0	2.7	6.6	5.9	0.0
		1.74	1.0	0.0	1.0	1.7	0.0	1.7	2.5	2.7	0.0
		15.00	0.7	0.0	0.7	0.5	0.0	0.5	1.4	1.2	0.0
Shear fracture (92.7% of the failure load)		0.00	6.0	7.5	13.5	7.9	4.2	12.1	28.1	13.9	11.7
		0.58	5.0	1.1	6.1	4.3	0.9	5.2	12.5	9.3	2.0
		1.16	4.9	0.9	5.8	3.6	0.7	4.3	11.6	8.5	1.6
		1.74	4.4	0.7	5.1	3.4	0.7	4.1	10.4	7.8	1.4
		2.32	5.0	0.3	5.3	3.4	0.4	3.8	10.5	8.4	0.7
		12.00	1.1	0.1	1.2	1.9	0.0	1.9	3.0	3.0	0.1
Shear fracture (after failure)		0.74[e]	7.3	6.7	14.0	7.2	2.7	9.9	27.6	14.5	9.4
		1.37[e]	6.8	4.9	11.7	7.5	1.8	9.3	23.7	14.3	6.7
		1.95[e]	5.6	4.2	9.8	6.9	2.3	9.2	20.6	12.5	6.5
		2.53[e]	6.6	1.4	8.0	6.9	0.9	7.8	17.0	13.5	2.3
		3.11[e]	4.7	1.0	5.7	5.7	0.9	6.6	12.7	10.4	1.9
		3.69[e]	6.4	0.6	7.0	6.0	0.5	6.5	14.7	12.4	1.1
		13.50[e]	1.1	0.1	1.2	1.2	0.1	1.3	2.6	2.3	0.2

Note. The first row "Intact" indicates the background microcrack density. The subsequent two rows of "Tensile fracture" and "Shear fracture" determine the microcrack density in the central damage zone (D = 0 mm) with respect to different stress levels. The bottom three rows summarize the microcrack density with respect to the distance away from the core of damage zones (D as the variable).
[a]The microcrack density is measured on the polished free surface of specimen. The possible variation of density with thickness has not been considered. [b]D is the distance between the center of the measured image and the center of damage zone. [c]BC = grain boundary crack; TC = transgranular crack. [d]Measurement is not performed on specimens subjected to 20% stress level since the damage zone is unobvious. [e]According to the analysis in section 3.4, the shear fracture is approximately 1.0 mm wide. The first image captured at the edge of the shear fracture is 578.7 μm wide; thus, the center of the image is about (0.24 + 0.5) mm from the center of the shear fracture. Calculations for the other data of distance are the same.

densities of grain boundary crack are about 9.0/mm, which is much higher than the total density of transgranular crack. This result agrees well with those observations illustrated in section 3.3. Additionally, it is worthwhile to note that measurements have only been conducted on specimens subjected to stress levels no less than 50% when continuous dominant microcracks have formed already (Figures 8c and 8d). There should be a transitional stage before 50% stress level that the microcrack density increases with the loading.

In the damage zones of shear fractures, the densities of grain boundary crack show neither increasing trend nor anisotropy trend with the increase of loading (Table 1 and Figure 13b). The total densities of grain boundary crack are about 11.0/mm, which are comparable to that in the damage zones of tensile fracture. On the contrary, the densities of transgranular crack show both increasing and anisotropy trends with the increase of loading (Figure 13b). The total microcrack density of transgranular crack jumps from 1.0/mm up to 10.5/mm when loading increases from 82.4% to 92.7% at which level transgranular crack density measured perpendicular to the σ_1 direction ($P_L^{\perp}$) is over two times of that measured parallel to the σ_1 direction ($P_L^{\parallel}$) (Table 1). This microcracking behavior is different from that of tensile fractures significantly.

Continuous measurements perpendicular to the damage zones support the conclusion that anisotropy is unobvious for grain boundary cracks throughout the damage zones (Figure 14a). However, the grain boundary crack density of tensile fracture at 90% stress level falls down sharply with the increase of distance from the damage zone center, while this value decreases slightly in shear fracture of 92.7% stress level and remains nearly constant in shear fracture after failure. It indicates that grain boundaries in the damage zone of a shear

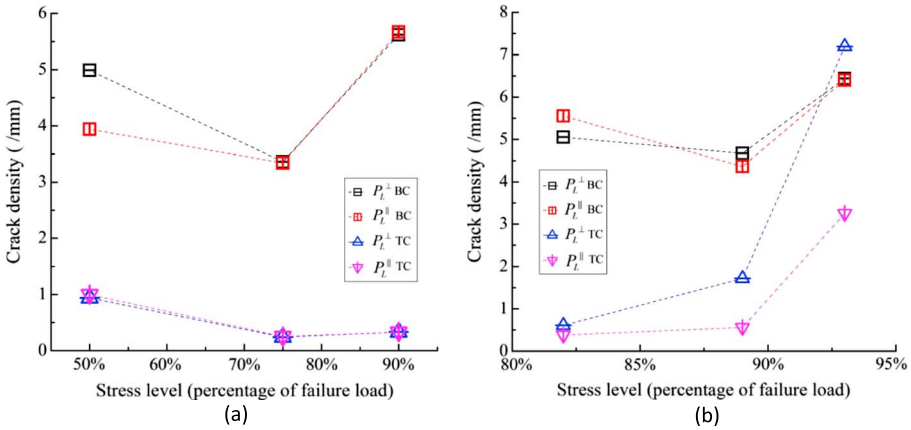

Figure 13. Microcrack densities ($P_L^{\parallel}$ and $P_L{}^{\perp}$) at different stress levels (percentage of failure load) of (a) tensile fracture and (b) shear fracture. In both plots, grain boundary crack (BC) and transgranular crack (TC) are represented by square and triangle symbols respectively.

fracture are damaged over a wider area with a more severe degree than those in the damage zones of a tensile fracture.

The data of transgranular cracks shows a different situation. With the increase of distance from the damage zone center, the transgranular crack density of tensile fracture of 90% stress level remains at a very low value; however, this value falls down sharply in shear fracture of 92.7% stress level and decreases progressively in shear fracture after failure (Figure 14b). In shear fracture of 92.7% stress level, the area of a high transgranular crack density is confined within a range about half of a millimeter from the damage zone center, while this range expands to over 3.0 mm in specimen after failure (Figure 14b). This condition suggests that after 92.7% loading, transgranular cracks continue to proliferate to produce a wider and more severe damage zone where a shear fracture finally forms in the central part. Furthermore, Figure 14b also indicates that anisotropy is only obvious in areas of a high transgranular crack density. When transgranular crack becomes rare, anisotropy becomes unobvious.

Additionally, in the damage zone of a shear fracture, the transgranular crack density decreases logarithmically with the distance away from the shear fracture center (Figure 15). This result agrees well with many field investigations of the relationships between the density of microfractures near faults and the distance from faults surface (Anders & Wiltschko, 1994; Mizoguchi & Ueta, 2013; Vermilye & Scholz, 1998). Also, Figure 15 shows that when comparing with the failed sample, the 92.7% loaded sample has a narrower damage zone and a steeper decrease in transgranular crack density with distance away from the shear fracture center. This situation is qualitatively consistent with the field and laboratory examinations on granitic rocks in which a narrower damage zone and a steeper decrease in microcrack density were

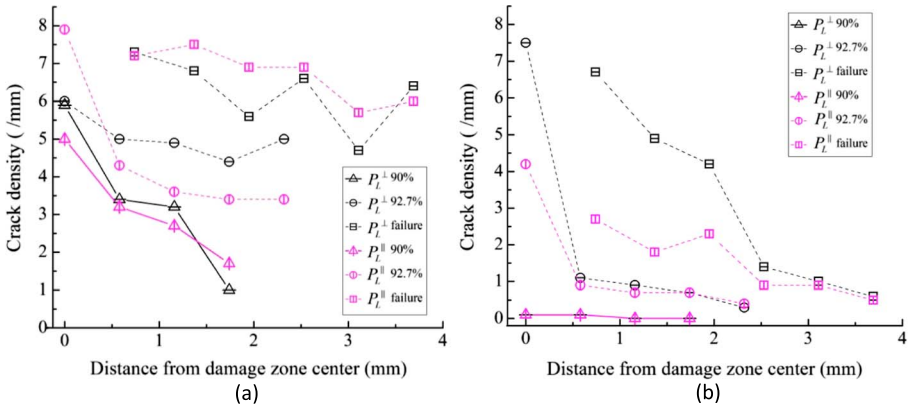

Figure 14. Microcrack densities ($P_L^{\parallel}$ and $P_L{}^{\perp}$) with respect to distance from the core of damage zones of tensile fracture of 90% stress level (triangle, solid line), shear fracture of 92.7% stress level (circle, dashed line), and shear fracture after failure (square, dashed line). (a) Grain boundary crack density. (b) Transgranular crack density.

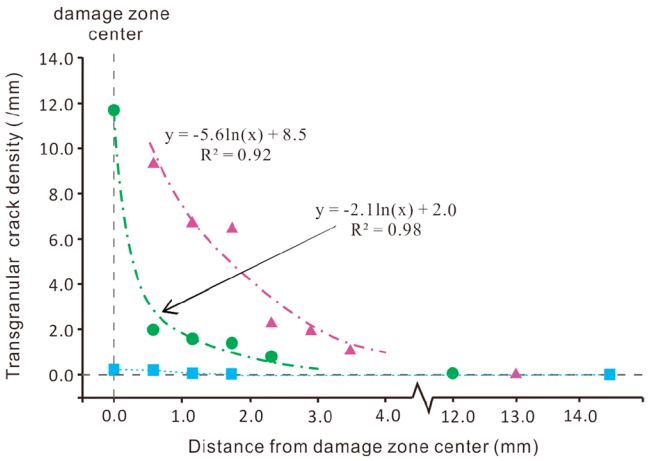

Figure 15. Transgranular crack densities with respect to distance from the center of damage zones of tensile fracture of 90% stress level (square), shear fracture of 92.7% stress level (disk), and shear fracture after failure (triangle).

reported with decreasing fault displacement (Mitchell & Faulkner, 2012). In these investigations, the microcrack density was of the same definition as in the present study, i.e., the total number of intersections per unit length of testing line. However, few other experimental observations provide similar results. A supporting observation was reported by Moore and Lockner (1995) in granite by defining the microcrack density as the total microcrack length in unit area. Nonetheless, they did not emphasize the different trend of decay of grain boundary cracks and transgranular cracks with distance. In the present study, by counting densities of grain boundary crack and transgranular crack separately, it seems that it is transgranular crack rather than grain boundary crack decreasing logarithmically with the distance away from the shear fracture center (Figures 14 and 15).

4. Discussion

4.1. Distinctions of Microscopic Characteristics of Tensile and Shear Fractures

Microscopic observations in the last section suggest that tensile and shear fractures have distinctly different microscopic characteristics. First, they have different development processes. The tensile fracture initiates as extensional microcracks at locations of tensile stress concentration, which then extend and widen as long dominant microcracks with wedge tip(s). Finally, these dominant microcracks develop into a tensile fracture. Although this process has not been captured continuously in the present microscopic observation, it can be inferred from the continuous camcorder recordings (Figure 5) and microscopic observation in later stages of loading (Figure 8). This inference is also supported by some other microscopic studies on tensile fractures (Wong & Einstein, 2009c; Zhao et al., 1995). On the contrary, the shear fracture initially appears as a damage zone containing abundant microcracks (Figures 6b and 11a). Then transgranular cracks nucleate to fragment mineral grains into small pieces with increasing loading, which is a critical stage for the development of a shear fracture in marble (Figures 11b–11d). Finally, a shear fracture, consisting of fragmented grains, transgranular cracks as well as grain boundary cracks, can be observed at an orientation of about 25° to those transgranular cracks which are subparallel with the loading direction (Figures 6d and 10). According to previous studies, a range of 10–30° is reported for the angle between the shear fracture and principal compression direction (Conrad & Friedman, 1976, Friedman et al., 1970, Menéndez et al., 1996, Moore & Lockner, 1995, Zhu et al., 2011), which agrees with the result obtained in this study.

Second, different microcrack types are involved in tensile and shear fractures. Tensile fracture is mainly composed of grain boundary cracks. Though a few transgranular cracks can be observed in the tensile fracture occasionally, their appearance shows little correlation with stress level (Figure 8). Different from tensile fractures, grain boundary cracks and transgranular cracks play the same important roles in the development of shear fractures (Figure 11). Specifically, transgranular cracks become increasingly popular as loading increases. Upon approaching the peak stress, the transgranular crack density is comparable with the grain boundary crack density (Figures 11c–11e). The above generalizations can also be drawn from Table 1 and Figure 13. Additionally, grain-scale surface spalling is also commonly observed in shear fractures. It shows a trend similar to that of transgranular cracks, i.e., the area of surface spalling increases as the loading increases (Figure 9).

Third, microcracks in tensile and shear fractures have different appearances. In tensile fractures, one or multiple long dominant microcracks of certain orientation often show a large extensional deformation of tens of microns. These dominant microcracks are usually flanked by microcracks of much smaller openings (Figure 8). It is why the linear white patch has an identifiable boundary with surrounding area (Figure 5). In shear fractures, however, long dominant microcracks are not observed before failure. Microcracks distribute uniformly within the damage zone, and they are generally of a length comparable to grain size. They are characterized by small openings of around only 1 μm before failure (Figures 10 and 11). It is why the diffuse white patch has an unclear boundary with surrounding area (Figure 6).

Fourth, tensile and shear fractures produce damage zones of different widths. Figure 8 suggests an approximate width of 300–1,000 μm for a tensile fracture damage zone, which encompasses about 2 to 6 calcite grains. In shear fractures, this width broadens with increasing loading and approaches 5.0 to 9.0 mm after failure (Figures 6 and 11e), which encompasses about 25 to 45 calcite grains. This point explains why the linear and diffuse white patches display different widths (Figures 5 and 6). This distinction in width between tensile fracture and shear fracture is also illustrated by a quantitative assessment of microcrack densities. In Table 1, the area of total microcrack density larger than 10/mm is confined within a width of 2×0.58 mm in tensile fracture, while this width is larger than 2×3.69 mm in shear fracture. Sagong and Bobet (2003) have observed a damage width of 10–20 μm and 100 μm for tensile fracture (wing crack) and shear fracture (secondary crack), respectively, in molded gypsum. Compared with our data obtained on Carrara marble, the trends are the same; i.e., the damage area of shear fractures is wider than that of tensile fractures, while the absolute widths of the shear fracture in these two rock types are very different. If we neglect the needle shape of gypsum grain and approximate the average grain size of gypsum as 6 μm (Sagong & Bobet, 2003; Wong & Einstein, 2009c), the widths of the tensile and shear fractures in gypsum are about 1–4 grains and 17 grains, respectively. In this sense, the results of Sagong and Bobet (2003) are also comparable with those in the present study.

Finally, anisotropy of microcrack density is observed in shear fracture but unobvious in tensile fracture. Figures 13 and 14 suggest that anisotropy can only be observed given a large transgranular crack density. Because transgranular cracks become abundant only in shear fractures loaded close to the peak stress, anisotropy can be observed only in shear fractures at a high stress level rather than in tensile fractures.

4.2. Microcrack Anisotropy

Anisotropy is dominantly attributed to the development of transgranular cracks. This phenomenon partly explains the results obtained in many other studies about the anisotropy in specimens undergoing brittle failure. It was observed that transgranular cracks usually nucleate after 70–90% loading of the specimen strength in many rock types (DiGiovanni et al., 2007; Fonseka et al., 1985; Menéndez et al., 1996; Tapponnier & Brace, 1976). Results in the present study also confirm this observation (Figures 11a–11c). Therefore, microcrack anisotropy in specimens of brittle failure is often unobvious until approaching peak stress when transgranular cracks flourish. For example, $P_L^{\perp}$ and $P_L^{\parallel}$ were of similar values for westerly granite at loadings less than 85% peak stress (Tapponnier & Brace, 1976; Wong, 1982), while $P_L^{\perp}$ is relatively larger than $P_L^{\parallel}$ at the peak stress (Moore & Lockner, 1995; Tapponnier & Brace, 1976). A similar situation was also observed in marble (Fredrich et al., 1989).

On the other hand, for some other rocks, such as highly porous sandstone (Menéndez et al., 1996) or fine-grained (about 10 μm) limestone (Vajdova et al., 2010), anisotropy is unobvious even at the peak stress. This is partly because both high porosity and fine-grained texture should have discouraged the nucleation of transgranular cracks (Tatami et al., 1997; Yasuda et al., 1993). Dunn et al. (1973) tested three suites of sandstone of porosities ranging from 1% to 27% to observe the formation of throughgoing fractures. They found that with higher porosity, grains in the fault zone are less fractured, and transgranular cracks are more abundant in rocks of lower porosity. Our observation in marble suggests that a large grain is more likely to be fractured by transgranular cracks than a small grain (not observed in ductile regime for limestone (Nicolas et al., 2017)). A typical example is shown in Figure 11c. A similar conjecture was also proposed by Conrad and Friedman (1976) on sandstone. A measurement conducted on Vienne granite, which has a grain size over 2000 μm, should support the conjecture above (Homand et al., 2000). The authors found a considerable anisotropy for $P_L^{\perp}$ (2.1/mm) and $P_L^{\parallel}$ (0.7/mm) even at 80% loading of strength, which indicates that a rock of large grain size tends to produce transgranular cracks and thus shows anisotropy at a relatively early loading stage.

4.3. Implications to Seismic Activity

Acoustic emission (AE) events, which radiate elastic waves in a manner similar to seismic events observed in earthquakes, are closely associated with the microcracking process of the material under compression (Fortin et al., 2009; Mlakar et al., 1993; Mongi, 1962; Ohnaka & Mogi, 1982; Scholz, 1968a; Stanchits et al., 2014). Observation on microcracks in this study thus provides an insight into the development of AE events in the faulting (shear fracturing) process. First of all, microcrack density in Table 1 suggests two possible

distinctions of AE events in shear fracturing compared to tensile fracturing. A shear fracturing first exhibits a larger total microcrack density and a wider damage zone than a tensile fracturing. Logically, the former will be accompanied by more seismic events. Meanwhile, as compared with tensile fracturing, a shear fracturing involves much more transgranular cracks. As a result, more energy should be released in the former since the energy release rate of transgranular crack is usually several times of that of grain boundary crack (Abdollahi & Arias, 2012; Alber & Hauptfleisch, 1999; Tatami et al., 1997; Yasuda et al., 1993). Under comparable conditions (rupture length, fluid pressure, temperature, etc.), a faulting rupture would produce events of larger magnitudes than a tensional rupture. These conditions may not be comparable for only a pair of tensile and shear fractures, but they could be statistically comparable for a large number of events either from an earthquake sequence or a laboratory faulting process. It is probably why some nearly pure shear aftershocks (with insignificant non-double-couple components) exhibit a larger magnitude than some other tensional aftershocks (with substantial positive non-double-couple components) in the 1999 Izmit earthquake (Stierle et al., 2014). Analyses on some other seismic events have shown similar relation between components and magnitude of events (Ito et al., 2004; Kumar et al., 2015). Some laboratory studies also have reported larger magnitudes for AE events of shear source as compared with those events of tensile source (Graham et al., 2010; Kwiatek et al., 2014). Therefore, because of the distinctions about the number and magnitude of events discussed above, it is likely that tensile events cannot be detected using standard seismic networks and what we observe is typically dominated by shear motions in the instant of faulting or sliding (Stanchits et al., 2011).

Furthermore, the microcrack density analysis as summarized in Table 1 reveals that during the preliminary faulting stage (about 70%–90% of the failure load), the number of microcracking events is moderate, which contribute to a moderate number of AE events. Also, microcracks at this period are mainly grain boundary cracks (Figures 13a and 13b) of a small energy release rate, the corresponding AE events thus tend to exhibit small magnitudes. When approaching the formation of a throughgoing fault (above 90% of the failure load), transgranular cracks of a large energy release rate flourish, which should raise the average magnitude of the new bloomed AE events significantly. Together with the flourish of transgranular cracks, the broadening gouge (densely microcracked zone) due to increasing loading (Figure 14) brings a conspicuous increase on the total microcracking events. This phenomenon should result in an abrupt increase of AE events. Despite the difference in setup for different research focuses, the above inference agrees with experimental observations on the development of AE event with respect to its number (Fonseka et al., 1985; Fortin et al., 2009; Kwiatek et al., 2014) and magnitude (Kwiatek et al., 2014; Ohnaka & Mogi, 1982). Similar tendency of AE development was also observed in stick-slip experiments, whereas the specific appearance is influenced by the friction of slip surface (Goebel et al., 2013; Kwiatek et al., 2014; Passelégue et al., 2017) as well as slip rate (Passelègue et al., 2016).

Such an increase of the components of large magnitudes with loading has been expressed as the noticeable decrease of b values with stress in the Gutenberg and Richter relation (Goebel et al., 2013; Lockner et al., 1991; Scholz, 1968b). Some studies have attributed this phenomenon to the possible appearance of large cracks. It seems more accurate to associate this phenomenon with the rapid development of transgranular cracks according to observations on Carrara marble in this study. A logical assumption is that the rapid development of transgranular cracks will promote the appearance of large cracks by connecting with formerly developed grain boundary cracks; the resultant large cracks thus tend to have a sawtoothed shape instead of smooth appearance breaking through many grains in straight. This assumption is supported by a continuous observation on a small fault in Tennessee marble (Olsson & Peng, 1976) and the appearance of large cracks in some other studies (Cheng et al., 2016; Dunn et al., 1973). Additionally, many cases that parallel transgranular cracks nucleated within a grain due to sliding on twin lamellae or possibly along the cleavage have been recently reported (Cheng et al., 2016). If these transgranular cracks nucleate simultaneously, comparable to type TTS event in hornblende schist suggested by Lei et al. (2000), the corresponding AE event can have a magnitude even larger than that event triggered by a single transgranular crack. This may be another source of the events of large magnitudes.

Although shear microcrack has not been mentioned in this study, many transgranular cracks have been nucleated due to shear movement along grain boundaries or twin lamellae according to the specific analysis on microcrack nucleation in marble (Cheng et al., 2016; Fredrich et al., 1989; Olsson & Peng, 1976). Similarly, transgranular cracks were reported to be attributed to sliding along fractures in sandstone (Conrad &

Friedman, 1976). The number of transgranular cracks is representative of the population of sliding events (shear events) along microscopic weak planes to some degree. Therefore, upon approaching shear fracturing, the considerable increase of transgranular cracks in this study should indicate an increase of shear events. This inference agrees with some AE recordings on specimens, which showed an increase of shear-type events as approaching shear fracturing (Lei et al., 2000; Stanchits et al., 2006; Stanchits et al., 2011). On the other hand, those weak planes usually are not identified as shear microcracks because (1) the shear movement in grain scale is difficult to identify due to the absence of clear indicator and negligible magnitude and (2) such weak planes usually show a minute opening after unloading which render their origin unclear. This fact partially explains why shear microcracks are seldom seen in faulting specimens in which nearly half of recorded AE events are of shear source (Fortin et al., 2009).

Additionally, in direction normal to a fault, our observation suggests that only the spatial decay of transgranular cracks (Figure 14b) rather than grain boundary cracks, follow a power law relation (Figure 14a). Considering the correspondence between microcrack type and its energy release rate, events of large magnitudes thus should decay more conspicuously than events of small magnitudes. Nonetheless, by counting all events together, an investigation on off-fault distribution of AE events displayed a power law decay of seismic activity with increasing distance from the fault core (Goebel et al., 2014). We believe that if all the counted AE events are divided into two groups by a threshold magnitude, the group above the threshold magnitude should decay more conspicuously than another group. If this proposal stands the future seismological investigations, the correlation between AE event amplitude and the source mechanism of microcracking could be clearer.

5. Conclusions

To examine the microcracking characteristics of tensile and shear fracturing in Carrara marble comprehensively, two series of specimens containing different artificial en echelon flaw configurations (β = 30° and β = 90°) are uniaxially loaded to different stress levels. As such, typical tensile and shear fractures are successfully obtained. Microscopic observations are then conducted on small specimens cut from the specimens of different degrees of damage. Observations in the present study clearly show that the tensile fracturing is distinct from the shear fracturing in many different aspects.

1. White patches, as process zones preceding the development of fractures, exhibit different development processes for different fracture types. A tensile fracture is characterized by the linear white patch while a shear fracture is characterized by the diffuse white patch. Their development has been described in detail in sections 3.2 and 4.1.
2. In the damage zone of a tensile fracture, microcracking behavior is mainly related to the development of grain boundary cracks. In contrast, besides grain boundary cracks, transgranular cracks and grain spallings are also abundant in the damage zone of a shear fracture.
3. The damage zone of a tensile fracture contains one or multiple long dominant microcracks of large extensional deformation, which are flanked by a few microcracks confined within a width about 300–1,000 μm (2–6 calcite grains). In the damage zone of a shear fracture, however, long dominant microcracks are not observed before failure. Microcracks distribute uniformly within the damage zone, and they are generally of a length comparable to grain size. They are characterized by small openings of around only 1 μm before failure. Shear fracture usually forms a severe damage zone of a width about 5.0–9.0 mm (25–45 calcite grains) after failure.
4. Transgranular crack density is always remarkably lower than grain boundary crack density in tensile fractures at all stress levels, while it becomes comparable with grain boundary crack density in shear fractures as the loading approaches the peak stress.
5. In the direction perpendicular to a shear fracture, the transgranular crack density decreases logarithmically with the distance away from the shear fracture center, while the grain boundary crack density decreases gradually.
6. Anisotropy ($P_L^{\perp} > P_L^{\parallel}$) is dominantly attributed to the development of transgranular cracks, which nucleate later than grain boundary cracks at a high stress level. This phenomenon partly explains why in specimens undergoing brittle failure, microcrack anisotropy usually tends to be unobvious until approaching peak stress.

7. The observed microcracking characteristics provide some probable explanations to some results obtained from seismological studies.

Acknowledgments
The data used are listed in Table 1 and shown in figures. The research was supported by the Singapore Academic Research Fund Tier 1 grant under project RG112/14 and the Nanyang Technological University start up grant (M4080115.030). The first author acknowledges the support from the Fundamental Research Funds for the Central Universities, China University of Geosciences (Wuhan) (162301132729) and the China National Natural Science Foundation (41702314). The second author also acknowledges the support from the University of Hong Kong start-up fund, the Seed Funding Program for Basic Research for New Staff at the University of Hong Kong, the Research Grant Council General Research Fund 2017/18 (grant 17303917), and the support of the "China University of Geosciences Scholar" Program (2017046). The authors appreciate the assistance from Varun Maruvanchery in performing the microscopic observation. Also, great thanks are given to the anonymous reviewers and Qi-Quan Xiong, the PhD student at NTU for their suggestions to discuss the results in a broader scope.

References

Abdollahi, A., & Arias, I. (2012). Numerical simulation of intergranular and transgranular crack propagation in ferroelectric polycrystals. *International Journal of Fracture*, *174*(1), 3–15. https://doi.org/10.1007/s10704-011-9664-0

Alber, M., & Hauptfleisch, U. (1999). Generation and visualization of microfractures in Carrara marble for estimating fracture toughness, fracture shear and fracture normal stiffness. *International Journal of Rock Mechanics and Mining Sciences*, *36*(8), 1065–1071. https://doi.org/10.1016/S1365-1609(99)00069-6

Anders, M. H., & Wiltschko, D. V. (1994). Microfracturing, paleostress and the growth of faults. *Journal of Structural Geology*, *16*(6), 795–815. https://doi.org/10.1016/0191-8141(94)90146-5

Bieniawski, Z. T. (1967). Mechanism of brittle fracture of rock : part ii—experimental studies. *International Journal of Rock Mechanics & Mining Sciences & Geomechanics Abstracts*, *4*(4), 407–423.

Bobet, A., & Einstein, H. H. (1998). Fracture coalescence in rock-type materials under uniaxial and biaxial compression. *International Journal of Rock Mechanics and Mining Sciences*, *35*(7), 863–888. https://doi.org/10.1016/S0148-9062(98)00005-9

Brace, W. F., & Bombolakis, E. G. (1963). A note on brittle crack growth in compression. *Journal of Geophysical Research*, *68*, 3709–3713. https://doi.org/10.1029/JZ068i012p03709

Bristow, J. (1960). Microcracks, and the static and dynamic elastic constants of annealed and heavily cold-worked metals. *British Journal of Applied Physics*, *11*(2), 81–85. https://doi.org/10.1088/0508-3443/11/2/309

Chen, G., Kemeny, J., & Harpalani, S. (1995). Fracture propagation and coalescence in marble plates with pre-cut notches under compression.

Cheng, Y., Wong, L. N. Y., & Maruvanchery, V. (2016). Transgranular crack nucleation in Carrara marble of brittle failure. *Rock Mechanics and Rock Engineering*, *49*(8), 3069–3082. https://doi.org/10.1007/s00603-016-0976-2

Cheng, Y., Wong, L. N. Y., & Zou, C. J. (2015). Experimental study on the formation of faults from en-echelon fractures in Carrara marble. *Engineering Geology*, *195*, 312–326. https://doi.org/10.1016/j.enggeo.2015.06.004

Conrad, R. E. II, & Friedman, M. (1976). Microscopic feather fractures in the faulting process. *Tectonophysics*, *33*(1-2), 187–198. https://doi.org/10.1016/0040-1951(76)90056-1

DiGiovanni, A., Fredrich, J., Holcomb, D., & Olsson, W. (2007). Microscale damage evolution in compacting sandstone. *Geological Society, London, Special Publications*, *289*(1), 89–103. https://doi.org/10.1144/SP289.6

Dunn, D. E., LaFountain, L. J., & Jackson, R. E. (1973). Porosity dependence and mechanism of brittle fracture in sandstones. *Journal of Geophysical Research*, *78*, 2403–2417. https://doi.org/10.1029/JB078i014p02403

Edmond, J., & Paterson, M. (1972). Volume changes during the deformation of rocks at high pressures. *International Journal of Rock Mechanics and Mining Science and Geomechanics Abstracts*, *9*(2), 161–182. https://doi.org/10.1016/0148-9062(72)90019-8

Eoin, R. (1988). En échelon vein array development in extension and shear. *Journal of Structural Geology*, *10*(1), 63–71.

Fonseka, G. M., Murrell, S. A. F., & Barnes, P. (1985). Scanning electron microscope and acoustic emission studies of crack development in rocks. *International Journal of Rock Mechanics and Mining Science and Geomechanics Abstracts*, *22*(5), 273–289. https://doi.org/10.1016/0148-9062(85)92060-1

Fortin, J., Stanchits, S., Dresen, G., & Gueguen, Y. (2009). Acoustic emissions monitoring during inelastic deformation of porous sandstone: Comparison of three modes of deformation. *Pure and Applied Geophysics*, *166*(5-7), 823–841. https://doi.org/10.1007/s00024-009-0479-0

Fredrich, J. T., Evans, B., & Wong, T. F. (1989). Micromechanics of the brittle to plastic transition in Carrara marble. *Journal of Geophysical Research*, *94*, 4129–4145. https://doi.org/10.1029/JB094iB04p04129

Friedman, M., Perkins, R. D., & Green, S. J. (1970). Observation of brittle-deformation features at the maximum stress of westerly granite and solenhofen limestone. *International Journal of Rock Mechanics and Mining Science and Geomechanics Abstracts*, *7*(3), 297–302. https://doi.org/10.1016/0148-9062(70)90043-4

Gehle, C., & Kutter, H. K. (2003). Breakage and shear behaviour of intermittent rock joints. *International Journal of Rock Mechanics and Mining Sciences*, *40*(5), 687–700. https://doi.org/10.1016/S1365-1609(03)00060-1

Goebel, T. H. W., Becker, T. W., Sammis, C. G., Dresen, G., & Schorlemmer, D. (2014). Off-fault damage and acoustic emission distributions during the evolution of structurally complex faults over series of stick-slip events. *Geophysical Journal International*, *197*(3), 1705–1718. https://doi.org/10.1093/gji/ggu074

Goebel, T. H. W., Schorlemmer, D., Becker, T. W., Dresen, G., & Sammis, C. G. (2013). Acoustic emissions document stress changes over many seismic cycles in stick-slip experiments. *Geophysical Research Letters*, *40*, 2049–2054. https://doi.org/10.1002/grl.50507

Graham, C. C., Stanchits, S., Main, I. G., & Dresen, G. (2010). Comparison of polarity and moment tensor inversion methods for source analysis of acoustic emission data. *International Journal of Rock Mechanics and Mining Sciences*, *47*(1), 161–169. https://doi.org/10.1016/j.ijrmms.2009.05.002

Griffith, A. A. (1924). The Theory of Rupture. In *Proceedings of the first International Congress for Applied Mechanics, Delft* (pp. 55–63).

Hadley, K. (1976). Comparison of calculated and observed crack densities and seismic velocities in westerly granite. *Journal of Geophysical Research*, *81*, 3484–3494. https://doi.org/10.1029/JB081i020p03484

Hoek, E. (1968). Brittle fracture of rock. In K. G. Stagg & O. C. Zienkiewicz (Eds.), *Chapter 4 in Rock Mechanics in Engineering Practice* (pp. 99–124). London: John Wiley.

Homand, F., Hoxha, D., Belem, T., Pons, M.-N., & Hoteit, N. (2000). Geometric analysis of damaged microcracking in granites. *Mechanics of Materials*, *32*(6), 361–376. https://doi.org/10.1016/S0167-6636(00)00005-3

Horii, H., & Nemat-Nasser, S. (1985). Compression-induced microcrack growth in brittle solids: Axial splitting and shear failure. *Journal of Geophysical Research*, *90*(B4), 3105–3125. https://doi.org/10.1029/JB090iB04p03105

Huang, J., Chen, G., Zhao, Y., & Wang, R. (1990). An experimental study of the strain field development prior to failure of a marble plate under compression. *Tectonophysics*, *175*, 269–284.

Ingraffea, A. R., & Heuze, F. E. (1980). Finite element models for rock fracture mechanics. *International Journal for Numerical and Analytical Methods in Geomechanics*, *4*(1), 25–43. https://doi.org/10.1002/nag.1610040103

Ito, Y., Matsubayashi, H., Kimura, H., Matsumoto, T., Asano, Y., & Sekiguchi, S. (2004). Spatial distribution for moment tensor solutions of the 2003 Tokachi-oki earthquake (M JMA = 8.0) and aftershocks. *Earth, Planets and Space*, *56*(3), 301–306. https://doi.org/10.1186/BF03353055

Julian, B. R., Miller, A. D., & Foulger, G. (1998). Non-double-couple earthquakes 1. Theory. *Reviews of Geophysics*, *36*, 525–549. https://doi.org/10.1029/98RG00716

Kranz, R. L. (1979). Crack growth and development during creep of Barre granite. *International Journal of Rock Mechanics and Mining Science and Geomechanics Abstracts*, *16*(1), 23–35. https://doi.org/10.1016/0148-9062(79)90772-1

Kumar, R., Gupta, S. C., & Kumar, A. (2015). Non-double-couple mechanism of moderate earthquakes occurred in Lower Siang region of Arunachal Himalaya: Evidence of factors affecting non-DC. *Journal of Asian Earth Sciences*, *98*, 105–115. https://doi.org/10.1016/j.jseaes.2014.10.025

Kwiatek, G., Goebel, T. H. W., & Dresen, G. (2014). Seismic moment tensor and b value variations over successive seismic cycles in laboratory stick-slip experiments. *Geophysical Research Letters*, *41*, 5838–5846. https://doi.org/10.1002/2014GL060159

Lajtai, E. (1971). A theoretical and experimental evaluation of the Griffith theory of brittle fracture. *Tectonophysics*, *11*(2), 129–156. https://doi.org/10.1016/0040-1951(71)90060-6

Lei, X., Kusunose, K., Rao, M. V. M. S., Nishizawa, O., & Satoh, T. (2000). Quasi-static fault growth and cracking in homogeneous brittle rock under triaxial compression using acoustic emission monitoring. *Journal of Geophysical Research*, *105*, 6127–6139. https://doi.org/10.1029/1999JB900385

Li, Y.-P., Chen, L.-Z., & Wang, Y.-H. (2005). Experimental research on pre-cracked marble under compression. *International Journal of Solids and Structures*, *42*(9-10), 2505–2516. https://doi.org/10.1016/j.ijsolstr.2004.09.033

Lockner, D. A., Byerlee, J. D., Kuksenko, V., Ponomarev, A., & Sidorin, A. (1991). Quasi-static fault growth and shear fracture energy in granite. *Nature*, *350*(6313), 39–42. https://doi.org/10.1038/350039a0

Menéndez, B., Zhu, W., & Wong, T.-F. (1996). Micromechanics of brittle faulting and cataclastic flow in Berea sandstone. *Journal of Structural Geology*, *18*(1), 1–16. https://doi.org/10.1016/0191-8141(95)00076-P

Mitchell, T. M., & Faulkner, D. R. (2012). Towards quantifying the matrix permeability of fault damage zones in low porosity rocks. *Earth and Planetary Science Letters*, *339*(Supplement C), 24–31.

Mizoguchi, K., & Ueta, K. (2013). Microfractures within the fault damage zone record the history of fault activity. *Geophysical Research Letters*, *40*, 2023–2027. https://doi.org/10.1002/grl.50469

Mlakar, V., Hassani, F. P., & Momayez, M. (1993). Crack development and acoustic emission in potash rock. *International Journal of Rock Mechanics and Mining Science and Geomechanics Abstracts*, *30*(3), 305–319. https://doi.org/10.1016/0148-9062(93)92732-6

Mongi, K. (1962). Study of the elastic shocks caused by the fracture of heterogeneous materials and its relation to earthquakes phenomena. *Bulletin of the Earthquake Research Institute*, *40*, 125–173.

Moore, D. E., & Lockner, D. A. (1995). The role of microcracking in shear-fracture propagation in granite. *Journal of Strucrural Geology*, *17*(1), 95–114. https://doi.org/10.1016/0191-8141(94)E0018-T

Myers, R., & Aydin, A. (2004). The evolution of faults formed by shearing across joint zones in sandstone. *Journal of Structural Geology*, *26*(5), 947–966. https://doi.org/10.1016/j.jsg.2003.07.008

Nicholson, R., & Pollard, D. D. (1985). Dilation and linkage of echelon cracks. *Journal of Structural Geology*, *7*(5), 583–590. https://doi.org/10.1016/0191-8141(85)90030-6

Nicolas, A., Fortin, J., Regnet, J., Verberne, B., Plümper, O., Dimanov, A., … Guéguen, Y. (2017). Brittle and semi-Brittle Creep of Tavel Limestone Deformed at Room Temperature. *Journal of Geophysical Research: Solid Earth*, *122*, 4436–4459. https://doi.org/10.1002/2016JB013557

Nolen-Hoeksema, R. C., & Gordon, R. B. (1987). Optical detection of crack patterns in the opening-mode fracture of marble. *International Journal of Rock Mechanics and Mining Science and Geomechanics Abstracts*, *24*(2), 135–144. https://doi.org/10.1016/0148-9062(87)91933-4

Ohnaka, M., & Mogi, K. (1982). Frequency characteristics of acoustic emission in rocks under uniaxial compression and its relation to the fracturing process to failure. *Journal of Geophysical Research*, *87*, 3873–3884. https://doi.org/10.1029/JB087iB05p03873

Olsson, W. A. (1974). Microfracturing and faulting in a limestone. *Tectonophysics*, *24*(3), 277–285. https://doi.org/10.1016/0040-1951(74)90012-2

Olsson, W. A., & Peng, S. S. (1976). Microcrack nucleation in marble. *International Journal of Rock Mechanics and Mining Science and Geomechanics Abstracts*, *13*(2), 53–59. https://doi.org/10.1016/0148-9062(76)90704-X

Passelègue, F., Spagnuolo, E., Violay, M., Nielsen, S., Di Toro, G., & Schubnel, A. (2016). Frictional evolution, acoustic emissions activity, and off-fault damage in simulated faults sheared at seismic slip rates. *Journal of Geophysical Research: Solid Earth*, *121*, 7490–7513. https://doi.org/10.1002/2016JB012988

Passelégue, F. X., Latour, S., Schubnel, A., Nielsen, S., Bhat, H. S., & Madariaga, R. (2017). Influence of Fault Strength on Precursory Processes During Laboratory Earthquakes. In M. Y. Thomas, T. M. Mitchell, & H. S. Bhat (Eds.), *Fault Zone Dynamic Processes: Evolution of Fault Properties During Seismic Rupture*. Hoboken, NJ: John Wiley, Inc. https://doi.org/10.1002/9781119156895.ch12

Peng, S., & Johnson, A. M. (1972). Crack growth and faulting in cylindrical specimens of chelmsford granite. *International Journal of Rock Mechanics and Mining Science and Geomechanics Abstracts*, *9*(1), 37–86. https://doi.org/10.1016/0148-9062(72)90050-2

Petit, J.-P., & Barquins, M. (1988). Can natural faults propagate under mode II conditions? *Tectonics*, *7*(6), 1243–1256. https://doi.org/10.1029/TC007i006p01243

Pollard, D. D., Segall, P., & Delaney, P. T. (1982). Formation and interpretation of dilatant echelon cracks. *Geological Socity of America Bulletin*, *93*(12), 1291–1303. https://doi.org/10.1130/0016-7606(1982)93%3C1291:FAIODE%3E2.0.CO;2

Sagong, M., & Bobet, A. (2003). Micro-fractographic characterization of tensile and shear cracks.

Scholz, C. H. (1968a). Microfracturing and inelastic deformation of rock in compression. *Journal of Geophysical Research*, *374*, 1417–1432. https://doi.org/10.1098/rsta.2015.0422

Scholz, C. H. (1968b). The frequency-magnitude relation of microfracturing in rock and its relation to earthquakes. *Nihon Naika Gakkai Zasshi the Journal of the Japanese Society of Internal Medicine*, *96*(9), 1909–1911.

Shen, B., Stephansson, O., Einstein, H. H., & Ghahreman, B. (1995). Coalescence of fractures under shear stresses in experiments. *Journal of Geophysical Research*, *100*, 5975–5990. https://doi.org/10.1029/95JB00040

Stanchits, S., Fortin, J., Gueguen, Y., & Dresen, G. (2009). Initiation and propagation of compaction bands in dry and wet Bentheim sandstone. *Pure & Applied Geophysics*, *166*(5–7), 843–868.

Stanchits, S., Mayr, S., Shapiro, S., & Dresen, G. (2011). Fracturing of porous rock induced by fluid injection. *Tectonophysics*, *503*(1-2), 129–145. https://doi.org/10.1016/j.tecto.2010.09.022

Stanchits, S., Surdi, A., Gathogo, P., Edelman, E., & Suarez-Rivera, R. (2014). Onset of hydraulic fracture initiation monitored by acoustic emission and volumetric deformation measurements. *Rock Mechanics and Rock Engineering*, *47*(5), 1521–1532. https://doi.org/10.1007/s00603-014-0584-y

Stanchits, S., Vinciguerra, S., & Dresen, G. (2006). Ultrasonic velocities, acoustic emission characteristics and crack damage of basalt and granite. *Pure and Applied Geophysics*, *163*(5-6), 975–994. https://doi.org/10.1007/s00024-006-0059-5

Stierle, E., Bohnhoff, M., & Vavryčuk, V. (2014). Resolution of non-double-couple components in the seismic moment tensor using regional networks—II: Application to aftershocks of the 1999 M_w 7.4 Izmit earthquake. *Geophysical Journal International*, *196*(3), 1878–1888. https://doi.org/10.1093/gji/ggt503

Tapponnier, P., & Brace, W. (1976). Development of stress-induced microcracks in westerly granite. *International Journal of Rock Mechanics and Mining Science and Geomechanics Abstracts*, *13*(4), 103–112. https://doi.org/10.1016/0148-9062(76)91937-9

Tatami, J., Yasuda, K., Matsuo, Y., & Kimura, S. (1997). Stochastic analysis on crack path of polycrystalline ceramics based on the difference between the released energies in crack propagation. *Journal of Materials Science*, *32*(9), 2341–2346. https://doi.org/10.1023/A:1018588620081

Underwood, E. E. (1970). *Quantitative stereology*. Reading, MA: Addison-Wesley.

Vajdova, V., Baud, P., Wu, L., & Wong, T.-F. (2012). Micromechanics of inelastic compaction in two allochemical limestones. *Journal of Structural Geology*, *43*, 100–117. https://doi.org/10.1016/j.jsg.2012.07.006

Vajdova, V., Zhu, W., Natalie Chen, T.-M., & Wong, T.-F. (2010). Micromechanics of brittle faulting and cataclastic flow in Tavel limestone. *Journal of Structural Geology*, *32*(8), 1158–1169. https://doi.org/10.1016/j.jsg.2010.07.007

Vavryčuk, V. (2002). Non-double-couple earthquakes of 1997 January in West Bohemia, Czech Republic: Evidence of tensile faulting. *Geophysical Journal International*, *149*(2), 364–373. https://doi.org/10.1046/j.1365-246X.2002.01654.x

Vermilye, J. M., & Scholz, C. H. (1998). The process zone: A microstructural view of fault growth. *Journal of Geophysical Research*, *103*, 12,223–12,237. https://doi.org/10.1029/98JB00957

Weiss, J., & Schulson, E. M. (2009). Coulombic faulting from the grain scale to the geophysical scale: Lessons from ice. *Journal of Physics D: Applied Physics*, *42*(21), 18.

Wong, L. N. Y., & Einstein, H. H. (2009a). Systematic evaluation of cracking behavior in specimens containing single flaws under uniaxial compression. *International Journal of Rock Mechanics and Mining Sciences*, *46*(2), 239–249. https://doi.org/10.1016/j.ijrmms.2008.03.006

Wong, L. N. Y., & Einstein, H. H. (2009b). Crack coalescence in molded gypsum and Carrara marble: Part 1. Macroscopic observations and interpretation. *Rock Mechanics and Rock Engineering*, *42*(3), 475–511. https://doi.org/10.1007/s00603-008-0002-4

Wong, L. N. Y., & Einstein, H. H. (2009c). Crack coalescence in molded gypsum and Carrara marble: Part 2. Microscopic observations and interpretation. *Rock Mechanics and Rock Engineering*, *42*(3), 513–545. https://doi.org/10.1007/s00603-008-0003-3

Wong, L. N. Y., & Maruvanchery, V. (2016). Different lithological varieties of Bukit Timah granite in Singapore: A preliminary comparison study on engineering properties. *Rock Mechanics and Rock Engineering*, *49*(7), 2923–2935. https://doi.org/10.1007/s00603-015-0825-8

Wong, R., Li, T., Chau, K., Li, S., & Zhu, W. (2007). Crack growth study of a 3-D surface fracture under compressions using strain and acoustic emission measurements. Symposium.

Wong, R. H., Guo, Y., Li, L., Chau, K., Zhu, W., & Li, S. (2006). Anti-wing crack growth from surface flaw in real rock under uniaxial compression. In *Fracture of Nano and Engineering Materials and Structures* (pp. 825–826). Dordrecht: Springer. https://doi.org/10.1007/1-4020-4972-2_408

Wong, R. H. C., & Chau, K. (1998). Crack coalescence in a rock-like material containing two cracks. *International Journal of Rock Mechanics and Mining Sciences*, *35*(2), 147–164. https://doi.org/10.1016/S0148-9062(97)00303-3

Wong, R. H. C., Leung, W. L., & Wang, S. W. (2001). Shear strength study on rock-like models containing arrayed open joints. Dc Rocks E U.S. Symposium on Rock Mechanics.

Wong, T.-F. (1982). Micromechanics of faulting in westerly granite. *International Journal of Rock Mechanics and Mining Science and Geomechanics Abstracts*, *19*(2), 49–64. https://doi.org/10.1016/0148-9062(82)91631-X

Wong, T.-F. (1985). Geometric probability approach to the characterization and analysis of microcracking in rocks. *Mechanics of Materials*, *4*(3-4), 261–276. https://doi.org/10.1016/0167-6636(85)90023-7

Wu, X. Y., Baud, P., & Wong, T.-f. (2000). Micromechanics of compressive failure and spatial evolution of anisotropic damage in Darley Dale sandstone. *International Journal of Rock Mechanics and Mining Sciences*, *37*(1-2), 143–160. https://doi.org/10.1016/S1365-1609(99)00093-3

Yang, S. Q., Dai, Y. H., Han, L. J., & Jin, Z. Q. (2009). Experimental study on mechanical behavior of brittle marble samples containing different flaws under uniaxial compression. *Engineering Fracture Mechanics*, *76*(12), 1833–1845. https://doi.org/10.1016/j.engfracmech.2009.04.005

Yang, S. Q., Jiang, Y. Z., Xu, W. Y., & Chen, X. Q. (2008). Experimental investigation on strength and failure behavior of pre-cracked marble under conventional triaxial compression. *International Journal of Solids and Structures*, *45*(17), 4796–4819. https://doi.org/10.1016/j.ijsolstr.2008.04.023

Yang, S. Q., Ranjith, P. G., Jing, H. W., Tian, W. L., & Ju, Y. (2017). An experimental investigation on thermal damage and failure mechanical behavior of granite after exposure to different high temperature treatments. *Geothermics*, *65*, 180–197. https://doi.org/10.1016/j.geothermics.2016.09.008

Yang, S. Q., Tian, W. L., & Ranjith, P. G. (2017). Experimental investigation on deformation failure characteristics of crystalline marble under triaxial cyclic loading. *Rock Mechanics and Rock Engineering*, *50*(11), 2871–2889. https://doi.org/10.1007/s00603-017-1262-7

Yasuda, K., Tatami, J., Asada, K., Matsuo, Y., & Kimura, S. (1993). Influence of crack propagation path on the fracture toughness of polycrystalline Al_2O_3. *Journal of the Ceramic Society of Japan*, *101*(1180), 1384–1389. https://doi.org/10.2109/jcersj.101.1384

Zhang, Z. N., Wang, D. Y., Zheng, H., & Ge, X. R. (2012). Interactions of 3D embedded parallel vertically inclined cracks subjected to uniaxial compression. *Theoretical and Applied Fracture Mechanics*, *61*, 1–11. https://doi.org/10.1016/j.tafmec.2012.08.001

Zhao, Y., Liang, H., Huang, J., Geng, J., & Wang, R. (1995). Development of subcracks between en echelon, fractures in rock plates. *Pure & Applied Geophysics*, *145*(3–4), 759–773.

Zhu, W., Baud, P., Vinciguerra, S., & Wong, T.-F. (2011). Micromechanics of brittle faulting and cataclastic flow in Alban Hills tuff. *Journal of Geophysical Research*, *116*, B06209. https://doi.org/10.1029/2010JB008046